ARTICLE

Check for updates

High cycle life all-solid-state fluoride ion battery with La$_2$NiO$_{4+d}$ high voltage cathode

Mohammad Ali Nowroozi[1], Kerstin Wissel [1], Manuel Donzelli[1], Niloofar Hosseinpourkahvaz[1], Sergi Plana-Ruiz[2,3], Ute Kolb[2,4], Roland Schoch [5], Matthias Bauer [5], Ali Muhammad Malik[1,6], Jochen Rohrer[6], Sergei Ivlev[7], Florian Kraus [7] & Oliver Clemens [1,8 ✉]

Fluoride ion batteries (FIBs) are a recent alternative all-solid-state battery technology. However, the FIB systems proposed so far suffer from poor cycling performance. In this work, we report La$_2$NiO$_{4.13}$ with a Ruddlesden-Popper type structure as an intercalation-based active cathode material in all solid-state FIB with excellent cycling performance. The critical charging conditions to maintain the conductivity of the cell were determined, which seems to be a major obstacle towards improving the cycling stability of FIBs. For optimized operating conditions, a cycle life of about 60 cycles and over 220 cycles for critical cut-off capacities of 50 mAh/g and 30 mAh/g, respectively, could be achieved, with average Coulombic efficiencies between 95 – 99%. Cycling of the cell is a result of fluorination/de-fluorination into and from the La$_2$NiO$_{4+d}$ cathode, and it is revealed that La$_2$NiO$_{4.13}$ is a multivalent electrode material. Our findings suggest that La$_2$NiO$_{4.13}$ is a promising high energy cathode for FIBs.

[1] Fachgebiet Materialdesign durch Synthese, Institut für Materialwissenschaft, Technical University of Darmstadt, Alarich-Weiss-Straße 2, 64287 Darmstadt, Germany. [2] Institut für Angewandte Geowissenschaften, Technical University of Darmstadt, Petersenstrasse 23, 64287 Darmstadt, Germany. [3] LENS, MIND/IN2UB, Departament d'Enginyeria Electrònica I Biomèdica, Universitat de Barcelona, Martí I Franquès 1, 08028 Barcelona, Catalonia, Spain. [4] Institut für Anorganische Chemie und Analytische Chemie, Johannes Guttenberg-Universität Mainz, Duesbergweg 10-14, 55128 Mainz, Germany. [5] Institute of Inorganic Chemistry and Center for Sustainable Systems Design (CSSD), Paderborn University, Warburger Straße 100, 33098 Paderborn, Germany. [6] Fachgebiet Materialmodellierung, Institut für Materialwissenschaft, Technical University of Darmstadt, Jovanka-Bontschits-Straße 2, 64287 Darmstadt, Germany. [7] Fachbereich Chemie, Philipps-Universität, Hans-Meerwein-Straße 4, 35043 Marburg, Germany. [8] Institut für Nanotechnologie, Karlsruher Institut für Technologie, Hermann-von-Helmholtz-Platz 1, 76344 Eggenstein-Leopoldshafen, Germany. ✉email: oliver.clemens@md.tu-darmstadt.de

The current market of portable energy storage systems is dominantly covered by lithium ion batteries (LIBs) due to their unique electrochemical performance including a high potential window, high energy density, reasonable capacity, and excellent cycle life[1–3]. While there is little concern about the shortage of reserves of elements in use on a short term, there is a controversy debate about the availability of sufficient reserves of critical elements (such as Li, Co) in long-term future, especially with the increase of electromobility and non-mobile energy storage technologies[4,5]. Further, owing to safety concerns there are needs for all solid-state batteries when it comes to future battery technologies[6,7]. Moreover, solid-state batteries can provide high energy density by using metal anode materials[8]. Therefore, scientific efforts were devoted to develop alternative (solid-state) battery technologies based on different shuttling ions and electrode materials, aiming to obtain similar performances as LIBs.

One of the alternatives that has been considered recently are so-called fluoride ion batteries (FIBs), which are based on the shuttling of fluoride ions. Since fluoride is the most stable anion with a high mobility[9], FIBs can theoretically provide a very wide potential window[10]. Apart from some limited reports on primary batteries based on fluoride ions in the 1970s[11,12], the first report on electrochemical rechargeable FIBs was proposed at 2011 by Fichtner et al.[13], based on an all-solid-state battery with $La_{0.9}Ba_{0.1}F_{2.9}$ as the solid electrolyte and conversion-based metal fluorides as active electrodes (e.g., CuF_2, BiF_3, and SnF_2 as the active cathode materials). Since then, the efforts on investigating such systems were further increased, addressing the development of solid[14–18] and liquid[19,20] electrolytes and improved cell designs[21,22] as well as the screening of conversion-based electrodes[23–26].

The principle advantage of conversion-based materials would lie in their high specific capacity (e.g., ~190 mAh/g for Bi/CeF_3, 270 mAh/g for $Bi/Mg-MgF_2$, and ~400 mAh/g for $Cu/Mg-MgF_2$ electrochemical cells); however, such systems suffer from a strong capacity fading for higher cycle numbers (for example, the capacity reduces to ~10% of its initial value after the first cycle for $Cu/Mg-MgF_2$)[13,24] and continuously thereafter. This can be explained from the fact that a conversion mechanism implies a huge degree of reorganization of the atoms on the transformation from a metal to a metal fluoride, with a change in the nature of the chemical bonds, and large volume changes[27] (the same holds true for conversion-based electrode materials for LIBs, for which nanotechnologies, such as thin films[2] or infiltration of conductive matrixes[28], are required for obtaining cycling stable conversion systems, although this still does not represent the state of the art of commercial systems). However, for some conversion systems such as Pb/PbF_2 and Zn/ZnF_2 within FIBs, comparably small volume changes and low melting temperatures of the corresponding metals facilitate a fair reversibility of those electrode systems[14,29], so they can be used as a reference if used in excess.

An alternative strategy for the design of electrode materials is to intercalate/deintercalate the ions into/from a host lattice, which drastically reduces volume changes. Such a strategy mainly leads to an improved structural and electrochemical reversibility, a lowering of overpotentials, and higher cycling stabilities[2,3]. In this respect, different oxides including perovskite-type $BaFeO_{2.5}$[30], schafarzikite-type MSb_2O_4[31], and the Ruddlesden–Popper-type ($A_{n+1}B_nO_{3n+1}$ or $AO(ABO_3)_n$) compounds $LaSrMnO_4$[32] and La_2CoO_4[33] as the cathode material and $Sr_2TiO_3F_2$[34] as the anode material have been previously considered mainly by our research group as potential host candidates for intercalation-based electrode materials for FIBs. The Ruddlesden–Popper-type structure type with $n = 1$ was so far found to be most suitable for the reversible intercalation of fluoride ions, explained by the presence of interstitial anion sites within the AO rock salt-related layers[35],

allowing for the insertion up to $2F^-$ ions per A_2BO_4 formula units[36]. Considering the capacity range of the state-of-the-art materials for LIBs (140 mAh/g for insertion/removal of 0.5 Li^+ ion into/from $LiCoO_2$[3], though the state of the art of $LiCoO_2$ has been recently enhanced by improving the structure and interface instability and therefore higher capacities have also been observed[37]), the theoretical capacities of 155 and 133 mAh/g for $LaSrMnO_4$ and La_2CoO_4, respectively, used for FIBs are comparable. Although structural reversibility could be confirmed for the compounds used so far, significant capacity fading can be observed over the cycling of the cells, though at a reduced rate compared to conversion-based compounds. In contrast to conversion-based systems, this does not originate from the volume changes on the intercalation of fluoride ions but from degradation processes of the carbon-based additives, which resulted in additional overpotentials and limited Coulombic efficiencies for such intercalation-based systems so far[33]. Therefore, the search for better intercalation compounds needs to go on. Density functional theory (DFT)-based calculations (reported within this manuscript) predicted La_2NiO_4 to serve as a high energy (high capacity and high potential) intercalation-based cathode material in FIBs with a fairly constant plateau around 1.5–1.7 V vs. Zn/ZnF_2 and a theoretical capacity of ~134 mAh/g (for intercalation of $2F^-$ ions: formation of $La_2NiO_4F_2$). Therefore, this material could serve as a new starting point for the search of reversible host materials for fluoride ions.

In this work, we report on the first all-solid-state FIB with high cycling stability and close to 100% Coulombic efficiency (average Coulombic efficiency of 97.68% and 95.44% for charge cutoff capacities of 30 and 50 mAh/g, respectively) over a large range of cycle numbers (>200) with operating times of >3 months. The cells are based on La_2NiO_{4+d} as a new high-voltage cathode material, $La_{0.9}Ba_{0.1}F_{2.9}$ as the solid electrolyte, and Pb/PbF_2 or Zn/ZnF_2 as the anode systems. Electrochemical impedance spectroscopy (EIS) and X-ray photoelectron spectroscopy (XPS) reveal that, although the carbon additive is affected within a side reaction on charging, stable cycling can be obtained on reducing the cutoff capacities with respect to the maximum capacity. In addition, the phase behavior of La_2NiO_{4+d} was found to be complex. Therefore, the $La_2NiO_{4+d}F_y$ fluorinated phase has been further investigated by means of transmission electron microscopy (TEM) techniques (imaging, automated diffraction tomography (ADT) and energy-dispersive X-ray (EDX) spectroscopy) together with X-ray absorption spectroscopy (XAS), confirming nearly full occupation of the interstitial sites by anions and successful formation of a high fluorine content phase of $La_2NiO_{4.13}F_{1.59}$.

Results and Discussion

Electrochemical charging and the fluorination behavior of La_2NiO_{4+d}. The compound La_2NiO_{4+d} formed after solid-state synthesis has an approximate composition of $La_2NiO_{4.13}$ ($d = 0.13$)[38]. From this, a theoretical maximum capacity of 125 mAh/g for the formation of $La_2NiO_{4.13}F_{1.87}$ can be expected if one assumes a simple filling of all empty interstitial anion sites, according to the following reaction equation:

$$La_2NiO_{4.13} + 1.87\,F^- \leftrightharpoons La_2NiO_{4.13}F_{1.87} + 1.87\,e^-.$$
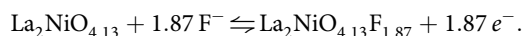
Schematic illustrations of the un-fluorinated $La_2NiO_{4.13}$ and fluorinated $La_2NiO_{4.13}F_{1.87}$ state have been plotted in Fig. 1.

As described in "Methods," the active La_2NiO_{4+d} cathode material has been mixed (and ball milled) with the $La_{0.9}Ba_{0.1}F_{2.9}$ electrolyte material and carbon nanotubes (CNTs) in order to improve the ionic and electronic conductivity of the cell, respectively. Supplementary Fig. 1 shows scanning TEM (STEM)

images of the synthesized cathode composite material before charge, which gives an indication that the electrolyte and CNTs agglomerate at the surface of the active cathode material. This is
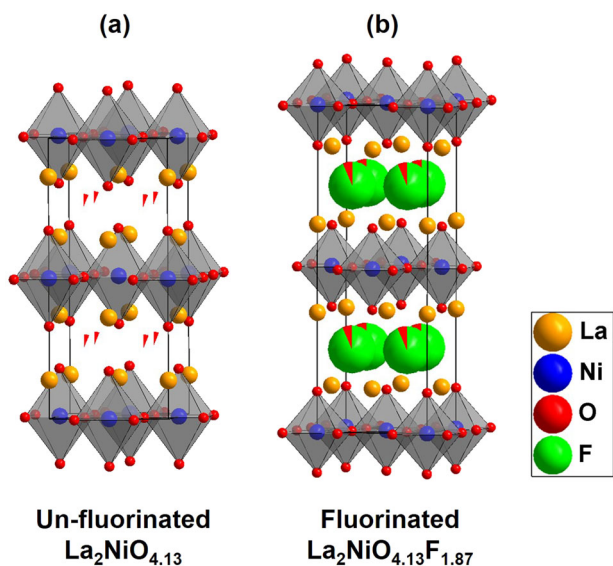
Fig. 1 Scheme of structural changes in La$_2$NiO$_{4.13}$. Schematic illustrations of the **a** un-fluorinated La$_2$NiO$_{4.13}$ and **b** the hypothetical fully fluorinated state La$_2$NiO$_{4.13}$F$_{1.87}$. Fractional occupancies are depicted for the interstitial anion site.

desirable from the ionic and electronic conductivity point of view. However, even partial coverage of the active cathode material by the solid electrolyte and the carbon additive prohibits a detailed analysis of the changes of the La$_2$NiO$_{4.13}$ particles on charging by means of surface-sensitive techniques such as XPS, since the spectra become strongly dominated by the carbon and electrolyte species (see "Discussion" within Supplementary Notes). In this respect, other techniques including Fast-ADT, EDX, and XAS were used in order to understand the structural changes of the La$_2$NiO$_{4+d}$ cathode material on charging the cell, which will be discussed later in this section.

In order to investigate the structural changes that are expected to occur on F$^-$ anion incorporation into Ruddlesden–Popper-type compounds during the electrochemical charging step, different La$_2$NiO$_{4+d}$/Zn-ZnF$_2$ cells were galvanostatically charged to various cutoff capacities up to 155 mAh/g. Figure 2a represents the charging curves showing excellent reproducibility regardless of the use of different cells. The charging curve can be divided into three regions. The starting potential of the La$_2$NiO$_{4+d}$/Zn-ZnF$_2$ cell is at about 0.8 V (start of the region (I)) followed by a sharp increase in the voltage up to ~1.7 V over a small capacity range of 10 mAh/g. Since the initiation of the electrochemical reaction often involves several steps including overcoming the chemical activation energy barrier, mass transfer, and adsorption of electroactive material[39], such an increase in overvoltage is reasonable. At 1.7 V, a fairly flat plateau with an increase to ~2.0 V over a capacity range of ~130 mAh/g can be observed (region (II)). In this region, strong structural changes are observed within the cathode composite with respect to the Ruddlesden–Popper phase. The respective XRD measurements
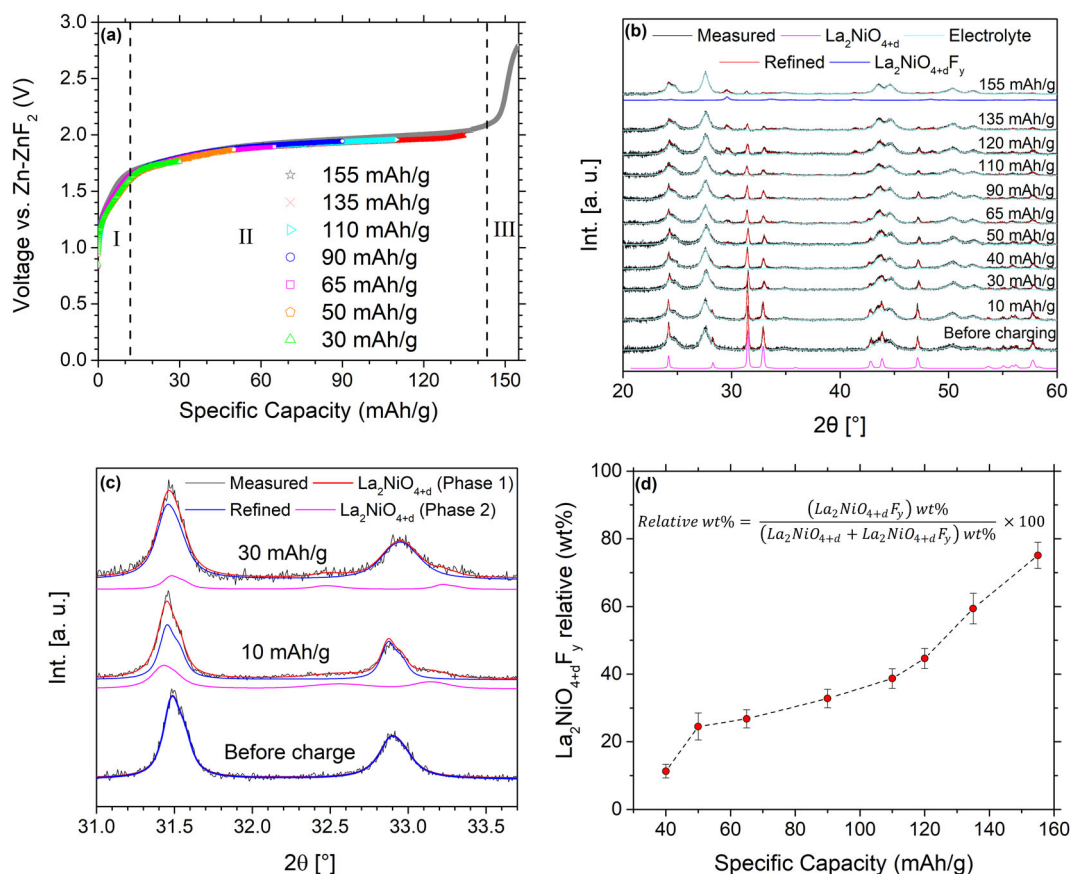
Fig. 2 Electrochemical fluorination of La$_2$NiO$_{4.13}$. a Galvanostatic electrochemical charging curves of the La$_2$NiO$_{4+d}$/Zn-ZnF$_2$ cell at different cutoff capacities at the operational temperature and current density of 170 °C and 24 μA/cm^2, respectively; **b, c** respective XRD patterns after the charging; **d** variations of the amount of the relative La$_2$NiO$_{4+d}$F$_y$ phase with respect to the charging cutoff capacity, according to the Rietveld analysis based on the obtained XRD data.

and corresponding lattice parameters after charging the La_2NiO_{4+d}/Zn-ZnF$_2$ cell to various cutoff capacities up to 155 mAh/g are plotted and listed in Fig. 2b–d and Table 1, respectively. The XRD pattern of the initial La_2NiO_{4+d} active cathode material before charging can be fitted in the tetragonal crystal system, space group $I4/mmm$[40] ($\sqrt{2}*a = \sqrt{2}*b = 5.4623(4)$ Å and $c = 12.6710(11)$ Å), which is the highest symmetry of the $n = 1$ Ruddlesden–Popper-type structure[35]. After electrochemical charging of the cell up to 10 mAh/g, two phases can be observed (Fig. 2c): the first phase is similar to the original La_2NiO_{4+d} with tetragonal unit cell and the second phase is an orthorhombic phase with increased lattice parameter a and decreased lattice parameter b (as shown in Fig. 2c), resulting from the small change in composition compared to the original La_2NiO_{4+d}. Owing to the fact that no superstructure reflections could be observed, all orthorhombic phases were refined using the highest symmetry orthorhombic space group of $Fmmm$, which can be derived from the aristotype $I4/mmm$ symmetry for a $\sqrt{2} \times \sqrt{2} \times 1$ supercell. Such an orthorhombic distortion was also found previously in $La_2NiO_3F_2$, which was prepared via a non-oxidative fluorination of La_2NiO_{4+d} using polyvinylidene fluoride[41] and resulted from ordering of vacancies, unresolvable within the composite mixtures used here. The orthorhombic distortion of this phase increases on further charging to 30 mAh/g (see Fig. 2c and Table 1), and the phase disappears at capacities >30 mAh/g. Then, a third $La_2NiO_{4+d}F_y$ (fluorine rich with orthorhombic space group $Fmmm$) phase can be found, where the large expansion of the c-axis ($c \sim 15.2$ Å compared to $c \sim 12.7$ Å for La_2NiO_{4+d}) is indicative for the strong fluorination of the material (see Fig. 2b, Supplementary Fig. 2a, and Table 1)[42–44]. The relative weight fraction of the $La_2NiO_{4+d}F_y$ phase increases with increasing charging capacity and reaches to approximately 77 wt-% at 155 mAh/g as is shown in Fig. 2d. Importantly, especially at the higher capacities within regions (II)/(III), a strong decrease of the overall amount of Ruddlesden–Popper phase compared to the $La_{0.9}Ba_{0.1}F_{2.9}$ solid electrolyte indicates a decomposition of the La_2NiO_{4+d} phase. It is also worth emphasizing that the XRD measurements do not indicate any significant decomposition of the $La_{0.9}Ba_{0.1}F_{2.9}$ electrolyte material (see Supplementary Table 1), which is plausible with respect to its wide electrochemical stability window reported previously[15] (ca. −1.8 to +3.7 V against Zn/ZnF$_2$).

Note that no significant structural changes can be detected in the anode material after charging (and also discharging) since the Zn-ZnF$_2$ anode material has been used in a high excess (see Supplementary Fig. 2b). This is in accordance with the previous studies on the M-MF$_2$ (M = Pb, Zn) anode materials for intercalation-based La_2CoO_4 cathode material for FIBs[27]. XPS measurement also does not show a significant change in the spectra of the anode material between the uncharged and charged (to 120 mAh/g) samples, as expected (please see Supplementary Fig. 3).

In addition, a partial oxidation of the carbon matrix[15,27,31–33] is overlying the charging of La_2NiO_{4+d} in region (II) ($U < \sim 2.1$ V) and proceeding within region (III) ($U > \sim 2.1$ V). This oxidation of the CNTs can also be detected by the XPS and Raman measurements, which will be fully discussed later with respect to the different changes happening within the CNT in the different regions. Therefore, a cutoff capacity of around 135 mAh/g must be considered to be the highest charging capacity before an extended destruction of the conductive carbon matrix takes place, which would result in an immediate deterioration of the discharge behavior[33].

Since the electrochemical fluorination of La_2NiO_{4+d} overlaps with these side reaction(s), determination of the fluorine content from the length of the charging plateau is not possible (e.g., as can be done for La_2CoO_4, with its separated plateau[33]). This is also evident from the low Coulombic efficiency within the first cycle,

Table 1 State of charge-dependent lattice parameters of the RP-type phase.

Cutoff capacity [mAh/g]	La$_2$NiO$_{4+d}$ (phase 1)/I4/mmm or Fmmm				La$_2$NiO$_{4+d}$ (phase 2)/Fmmm				La$_2$NiO$_{4+d}$F$_y$/Fmmm			
	a [Å]	b [Å]	c [Å]	V [Å³]	a [Å]	b [Å]	c [Å]	V [Å³]	a [Å]	b [Å]	c [Å]	V [Å³]
Before charge	5.462 (1)		12.671 (1)	378.1 (1)								
10	5.460 (1)		12.680 (1)	378.1 (1)	5.516 (2)	5.420 (1)	12.686 (3)	379.3 (2)				
30	5.453 (1)		12.715 (2)	378.2 (1)	5.526 (2)	5.406 (2)	12.665 (5)	378.4 (2)				
40	5.455 (1)		12.727 (2)	378.7 (1)					5.370 (9)	5.309 (8)	15.199 (30)	433.3 (13)
50	5.443 (1)	5.465 (1)	12.733 (2)	378.8 (1)					5.360 (8)	5.310 (8)	15.255 (30)	434.1 (13)
65	5.444 (1)	5.468 (1)	12.748 (2)	379.5 (1)					5.374 (5)	5.318 (4)	15.205 (16)	434.5 (7)
90	5.447 (1)	5.462 (1)	12.742 (2)	379.1 (1)					5.362 (3)	5.311 (3)	15.199 (12)	432.8 (5)
110	5.438 (1)	5.464 (1)	12.743 (3)	378.6 (1)					5.358 (3)	5.303 (3)	15.227 (11)	432.6 (5)
120	5.440 (1)	5.466 (1)	12.757 (3)	379.4 (1)					5.363 (2)	5.307 (3)	15.229 (10)	433.4 (4)
135	5.444 (1)	5.466 (1)	12.755 (3)	379.6 (2)					5.357 (2)	5.308 (3)	15.253 (10)	433.7 (4)
155	5.449 (1)	5.466 (1)	12.761 (4)	380.1 (2)					5.361 (2)	5.303 (3)	15.248 (9)	433.5 (4)

RD structural data of the La_2NiO_{4+d} active cathode material after charged up to different cutoff capacities at $T = 170$ °C and current density of 24 µA/cm².
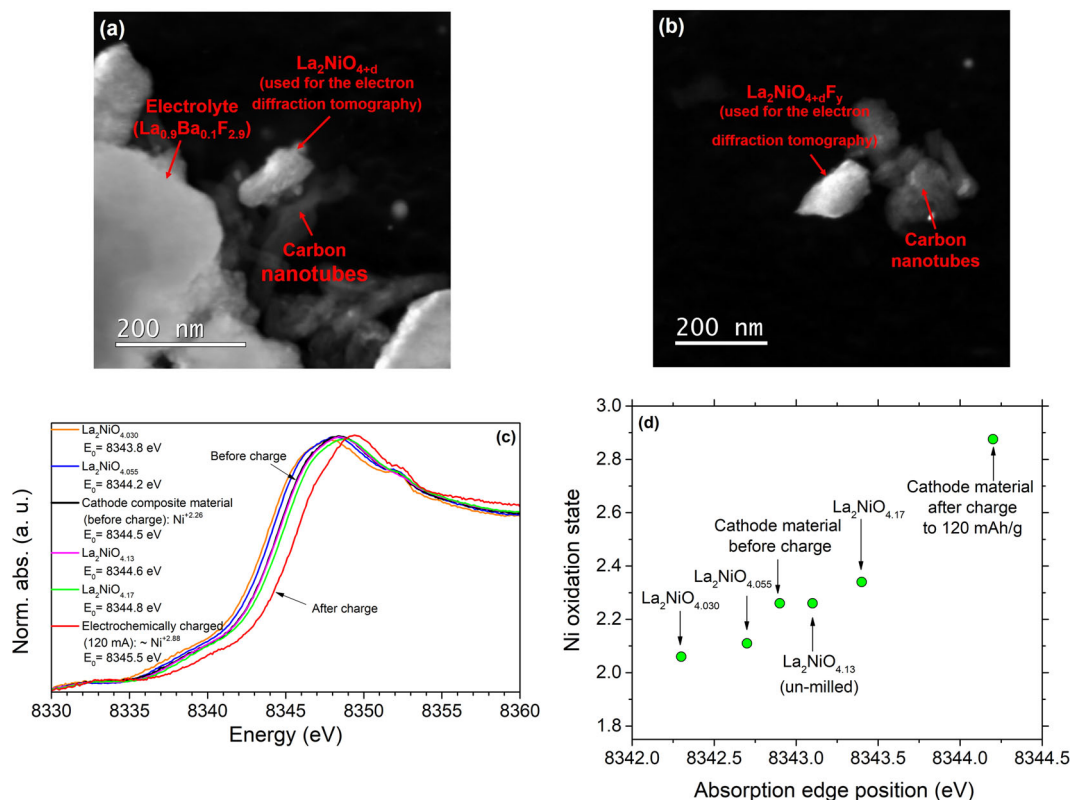
Fig. 3 Structure determination of selected particles and determination of average oxidation state of Ni. HAADF-STEM images of the cathode composite material after charge up to 120 mAh/g (at $T = 170\,°C$ and $I_{ch} = +24\,\mu A/cm^2$) showing the **a** un-fluorinated phase (La_2NiO_{4+d}) and **b** the fluorinated phase ($La_2NiO_{4+d}F_y$), which have been used for the Fast-ADT experiments. **c** The absorption edge energies of La_2NiO_{4+d} ($0.030 \leq d \leq 0.17$) as compared to the $La_2NiO_{4+d}F_y$ (after electrochemical fluorination up to 120 mAh/g with a current density of $+24\,\mu A/cm^2$ at 170 °C) in agreement with the results of electron diffraction analysis, EDX, and DFT calculations; **d** changes in the Ni oxidation state with respect to the absorption edge energies.

as is shown previously. Redox titrations of phase pure chemically fluorinated samples would be the method of choice for determining the fluorine content of the samples and average Ni oxidation state. Attempts were made to prepare phase pure fluorinated phase ($La_2NiO_{4+d}F_y$) by means of a variety of oxidative fluorination methods (mild fluorination reactions using CuF_2 in oxygen (see Supplementary Fig. 4a) as well as F_2 gas at various concentrations, reaction times, and temperatures (see Supplementary Fig. 4b, c). Regardless of the approach used, we could not form high amounts of the fluorinated phase with lattice parameter c of ~15.2 Å (for more information, please see Supplementary Notes). Further, XPS methods did not serve to analyze the change of the Ni oxidation state due to the strong surface coverage of the $La_2NiO_{4.13}$ particles with electrolyte and carbon additive (see the XPS results described in the Supplementary Information). Instead a new approach was used to analyze the fluorinated (charged) state of La_2NiO_{4+d} with respect to fluorine content and Ni oxidation state, which combines electron diffraction tomography (Fast-ADT), EDX, and XANES analysis.

Figure 3 shows the high-angle annular dark field (HAADF)-STEM images of the cathode composite material after charging up to 120 mAh/g. In agreement with the XRD measurements, two different phases of the Ruddlesden–Popper-type compound could be identified. Figure 3a depicts a single crystal of a nearly un-fluorinated La_2NiO_{4+d} (with $c \sim 12.67$ Å) after charge that is surrounded by CNTs and the $La_{0.9}Ba_{0.1}F_{2.9}$ electrolyte, whereas a well-isolated particle of $La_2NiO_{4+d}F_y$ ($c \sim 15.2$ Å) could be observed, which is shown Fig. 3b. Both crystals were further analyzed by EDX and electron diffraction tomography using the

Fast-ADT technique (more information about the ADT technique can be found in literature[45]).

The reconstruction of the observed diffraction space allowed the identification of the unit cell in the orthorhombic setting for both crystals: $a = 5.50$ Å, $b = 5.47$ Å, $c = 12.63$ Å for the un-fluorinated phase (La_2NiO_{4+d}), and $a = 5.37$ Å, $b = 5.31$ Å, $c = 14.45$ Å for the fluorinated phase ($La_2NiO_{4+d}F_y$). Supplementary Fig. 5 shows the projections of the reconstruction of the observed diffraction space along the main axes of the fluorinated phase that allowed the determination of the cell. These results well confirm the expansion of the cell along the c axis (contraction of the a and b axes) on fluorine insertion at the interstitial sites of the La_2NiO_{4+d} host. This is in a good agreement with the changes in the lattice parameters obtained by the XRD measurements (see Table 1), if we take into account that lattice parameters from electron diffraction are less accurate because of the camera length variation due to the electromagnetic lenses.

The quality of the Fast-ADT data was good enough for crystal structure determination through direct methods and further refinement within the space group *Fmmm*. Structure refinement using the dynamical scattering theory[46] was possible for the un-fluorinated phase but the reflection quality of the fluorinated phase only allowed to perform a kinematical refinement. Nevertheless, both crystal refinements converged with good and acceptable R1 values for electron diffraction (see Supplementary Table 2 for further details; structural parameters extracted from the refinement can be found in Supplementary Table 3). The degree of fluorination can be approximated from the refined interlayer occupancy indicating a composition of $La_2NiO_4X_{1.72}$

Table 2 Bond distances of Ni-O.

	La$_2$NiO$_4$ calculated	Un-fluorinated particle from Fast-ADT	La$_2$NiO$_4$F calculated	La$_2$NiO$_4$F$_2$ calculated	Fluorinated particle from Fast-ADT
$d_{equatorial}$ (Å)	1.94	1.93	2.01	1.97	1.89
d_{apical} (Å)	2.24	2.17	2.05	1.88	1.90
$d_{average}$ (Å)	2.09	2.05	2.03	1.93	1.90

The values given are based on the structural models determined via Fast-ADT and from DFT-based calculations.
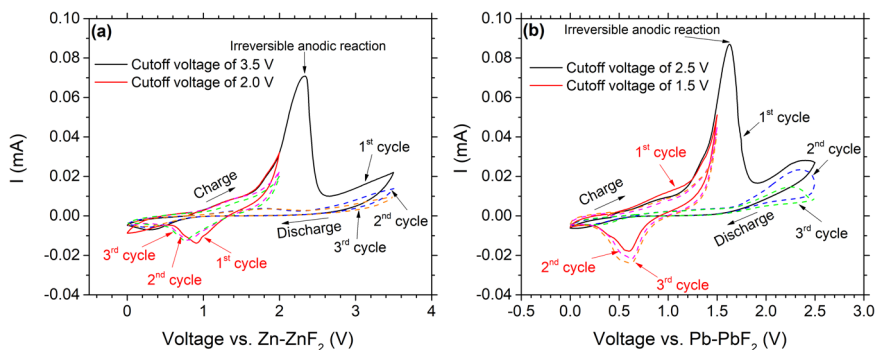
Fig. 4 CV measurements on La$_2$NiO$_{4.13}$. a Cyclic voltammograms of La$_2$NiO$_{4+d}$ vs. Zn-ZnF$_2$; **b** cyclic voltammograms of La$_2$NiO$_{4+d}$ vs. Pb-PbF$_2$. Both measurements were performed by a scan rate = 0.1 mV/s at T = 170 °C.

for the fluorinated phase, which corresponds to a Ni oxidation state of ~+3.85 for $d = 0.13$ (La$_2$NiO$_{4.13}$F$_{1.59}$) and +3.72 for $d = 0$ (La$_2$NiO$_4$F$_{1.72}$). In contrast, the interstitial site was found to be unoccupied for the un-fluorinated particle. This agrees well with the complementary elemental analyses via EDX, from which compositions of La$_2$Ni$_{1.04}$O$_{3.8}$F$_{1.8}$ (nearly fully filled interstitial sites) and La$_2$NiO$_4$ (nearly empty interstitial sites) can be approximated for fluorinated and un-fluorinated crystals, respectively (please see Supplementary Fig. 6 and Supplementary Table 4). XAS indicates a clear shift in the absorption spectrum to higher energies for the charged sample in comparison to uncharged (La$_2$NiO$_{4.13}$), as can be seen in Fig. 3c, d (detailed X-ray absorption edges can be found in Supplementary Table 5). Furthermore, reference samples of known compositions and oxidation states are also plotted for comparison (please see Supplementary Table 6 for the composition of the reference samples). This energy shift (~1.3 eV, see Fig. 3c, d) matches well with what would be expected from the average oxidation state after charging (which can be determined from the refined phase fractions and the average oxidation states estimated from the crystallographic analysis of Fast-ADT). The absence of changes between the spectra in the prepeak area as well as in the whiteline also indicates a similar coordination geometry of Ni and therefore a pure electronic effect (change in oxidation state), which causes the energy shift of the spectra.

DFT structure optimizations were performed for the different compositions La$_2$NiO$_4$F$_x$ (0 ≤ x ≤ 2, Δ = 0.5) and show that the c-axis tends to increase more strongly for fluorination degrees x > 1, reaching a value of ~15.2 Å for x = 2 (see Supplementary Fig. 7a). In addition, the contraction within the a/b-plane is also confirmed by this method. The changes of the axes are accompanied by strong changes of the bond distance of the apical oxygen ion to the Ni cation (Supplementary Fig. 7b). Remarkably, the calculated Ni–O distances agree well with the Ni–O distances from the Fast-ADT structural analysis (see Table 2). Further, the average bond distances are in excellent agreement with what would be expected from the sum of ionic radii[47] for divalent (2.09 Å) and tetravalent Ni (1.88 Å).

The DFT calculations further predict fairly similar potentials for the redox couple La$_2$NiO$_4$/La$_2$NiO$_4$F$_x$ (0 ≤ x ≤ 2) independent on the exact values of x (Supplementary Fig. 7c). This potential is about 0.3–0.5 V higher than the potential of La$_2$CoO$_4$/La$_2$CoO$_4$F$_{1.2}$[27,33]. This results in an increase of the energy density of La$_2$NiO$_4$ compared to La$_2$CoO$_4$. LaSrMnO$_4$ in principle also allows for the insertion of approximately two fluoride ions per formula unit[32,36]; however, the second fluoride ion can be only inserted at far higher potentials, which shows a severe destruction of the carbon additive, and makes this second plateau practically inaccessible for reversible battery applications (for a detailed discussion of the role of the carbon additive, see next section).

Determination of optimized charging conditions. To be able to optimize the cycling conditions of the cell, we aimed to gain a deeper understanding of the charging and discharging behavior by means of cyclic voltammetry (CV) and EIS.

The cyclic voltammograms for a La$_2$NiO$_{4+d}$/Zn-ZnF$_2$ cell show a broad peak at around 2.4 V, only in the forward direction of the first cycle, with a shoulder at lower potentials of around 1.8–2 V and a tail to as low as ~1 V. The broad peak at 2.4 V corresponds to an irreversible anodic (side) reaction during the charging step (Fig. 4a), and in case of the occurrence of the irreversible anodic reaction, no cathodic peak can be observed in the backward direction. However, limiting the cycling potential range to 2 V (see Fig. 4a) results in the observation of a reversible cathodic peak at ~1 V in the backward direction (see again Fig. 4a). A similar behavior is also observed when Pb-PbF$_2$ (see Fig. 4b) is used as the counter electrode (anode material), where the corresponding peaks occur at potentials reduced by ca. 0.4 V (the cathodic peak can be seen around ~0.6 V for Pb-PbF$_2$) due to the higher potential of this anode system compared to Zn/ZnF$_2$ (Fig. 4b). Unlike batteries that use a liquid electrolyte, it is not possible to construct a three-electrode set-up within the heated battery system used within this study. Therefore, CV experiments must be performed in such a way that the counter electrodes (anode materials) were used as reference electrodes. This explains the potential shifts observed for measurements against Zn-ZnF$_2$

in comparison to measurements against Pb-PbF$_2$ (the cyclic voltammograms basically coincide if corrected by the standard potential of M/MF$_2$ (M = Pb, Zn) derived from the formation energies given in ref. [9], see Supplementary Fig. 8). Since both, La$_2$NiO$_{4+d}$/Pb-PbF$_2$ and La$_2$NiO$_{4+d}$/Zn-ZnF$_2$ cells were cycled to 0 V as the lowest potential, this implies different degrees of de-fluorination after the first cycle. Therefore, different degrees of de-fluorination in combination with achieving identical CV conditions for both cells could explain the cathodic peak shift for the La$_2$NiO$_{4+d}$/Zn-ZnF$_2$ cell (Fig. 4a) for higher cycles, which was not observed for the La$_2$NiO$_{4+d}$/Pb-PbF$_2$ cell (Fig. 4b).

Further, the CNTs seem to be quite stable at potentials below ~1.3 V (against Pb-PbF$_2$ anode material; ~1.9 against Zn-ZnF$_2$ based on the difference (~0.6 V[9]) in the standard potentials of Pb/Pb^{+2} and Zn/Zn^{2+}) according to the cyclic voltammogram of a pure carbon-based cathode (Supplementary Fig. 9). An irreversible anodic peak can also be observed at ~2.1 V in the cyclic voltammogram of C/Pb-PbF$_2$, which corresponds probably to carbon oxidation. It is worth noting that the observed irreversible anodic peak in the cyclic voltammogram of C/Pb-PbF$_2$ can also be observed in the cyclic voltammograms of La$_2$NiO$_{4+d}$/Pb-PbF$_2$ and La$_2$NiO$_{4+d}$/Zn-ZnF$_2$ cells (Fig. 4). Further, it can be assumed that the peak shifts toward the lower potential range shows the catalytic effect of the La$_2$NiO$_{4+d}$ compound for carbon oxidation[32].

In order to have a better understanding on the nature of the irreversible anodic reactions on the carbon additive observed via CV, galvanostatic impedance spectroscopy has been performed for the La$_2$NiO$_{4+d}$ cell against Zn-ZnF$_2$ (see Fig. 5a, b; similar behavior is observed for charging against Pb-PbF$_2$, see Supplementary Fig. 10a, b) during the first charging step. It can be seen that the Nyquist plots of the La$_2$NiO$_{4+d}$/Zn-ZnF$_2$ cell at low charging capacities consist of a semicircle at high frequencies (>10 kHz) corresponding to the impedance of the solid electrolyte and interface resistance between the electrolyte and the electrode material[27] followed by a straight line with a slope of ~1 at frequencies <10 Hz arising from the diffusion processes within the active electrode materials[48], often referred to Warburg impedance[49] (Fig. 5b). This type of Nyquist plots are similar to what has been observed[27,33] for La$_2$CoO$_4$ against conversion-based anodes. It is worth emphasizing that the semicircles corresponding to the solid electrolyte and interface resistances cannot be resolved, which can also be seen from the BODE plots shown in Supplementary Fig. 11. The model, which can be used for fitting the Nyquist curves for capacities below ~130 mAh/g (corresponds to ~2 V), are labeled as "Model 1" in Supplementary Fig. 10c and consist of an RC circuit in series with a constant phase element (CPE) to describe the solid electrolyte plus interface resistance as well as the diffusion of fluoride ions into the electrode materials, respectively. For charging capacities belonging to potentials higher than ~2.0 V (higher than ~130 mAh/g), the slope of the straight line at low frequencies increases rapidly once the potential of the cell increases sharply, which is indicative for the development of a capacitive behavior of the cell. Then a different fit model (labeled as "Model 2" in Supplementary Fig. 10c) needs to be used, which differs from the first model by the use of a second resistance R_2 in parallel to the CPE.

The changes of the exponent α of the CPE on proceeded charging is plotted in Fig. 5a, confirming the capacitive behavior on transition from region (II) to region (III), and in agreement with the CV studies. More explanations about the CPE can be found in Supplementary Notes. In fact, the values of the exponent α appears to be around 0.5 within region (II), which is indicative for a Warburg-type behavior, while the α values rapidly increase up to 0.8 at region (III). It also needs to be particularly emphasized that this behavior does not appear within region (II)

and therefore cannot correspond to the partial decomposition of the active cathode material observed from the reduction of the Ruddlesden–Popper reflections by XRD.

To highlight the role of the carbon additive, we performed XPS measurements of the C1s emission line. On extended charging in region (III), additional broad high energy signals are appearing, in addition to a shift of the binding energy of the main sharp carbon signal by approximately 0.5 eV, which already occurs in region (II) (see Fig. 5c, d). This indicates an increasing oxidation (fluorination) of the carbon (or of a neighboring carbon atom)[50,51]. To visualize this oxidation, we represented the changes of carbon by a single parameter, which we calculated as the area-weighted average binding energy of each C1s emission line. This weighted binding energy increases strongly with increased charging (see Fig. 5d). The partial fits for all samples are shown in Supplementary Fig. 12 (details on the fitting procedure can also be found in Supplementary Notes together with additional partial spectra shown in Supplementary Fig. 13, which are dominated by the electrolyte and carbon signal).

The change of the carbon additive on charging is also reflected by using spectroscopical methods. The Raman spectra of pristine CNTs (before milling) and the samples before and after charging to 120 and 400 mAh/g can be found in Fig. 5e (the spectra were normalized to the maximum intensity of the D band in the respective spectrum). The observed bands are characteristic for carbonous materials. The G band is present in all graphene and graphitic materials and is originating from bond stretching of sp^2 hybridized carbon atoms. Owing to the presence of defects and disorder (i.e., everything which would lower the crystalline symmetry of the quasi infinite graphene lattice), the D (D for defect) and D' bands are observed. Second-order Raman scattering is found at higher Raman shifts[52]. The formation of disorder (e.g., by defects induced during milling or in the form of oxidized C species on charging) is well represented by the changes in the integral intensity ratio of the D and G bands[53,54]. As shown in Fig. 5f, additional disorder due to milling/charging leads to a considerable intensity increase of the D mode, while the intensity of the G band decreases. The highest I_D/I_G ratio was found for the sample charged to 400 mAh/g, which lies in region (III) and is therefore significantly overcharged, whereas at the end of region (II), the I_D/I_G ratio is more similar to the defect state, which was obtained after milling.

From the experiments performed, one can derive a more detailed picture on the potential-dependent structure and fluorine distribution on the CNTs. It is clear that the degree of oxidized (fluorinated) species increases within region (II) and (III); parts of the CNTs are already oxidized at potentials where the fluorination of La$_2$NiO$_{4.13}$ also takes place, i.e., within region (II), but within this range no strong increase in the impedance of the cell can be observed. At the transition to region (III) as well as within region (III), there seems to be a change in the principle impedance behavior of the cell (change from resistive to capacitive), which would imply that in this region the electrical conductivity of the CNT must be severely deteriorated. This can be correlated with previous studies: (1) Li et al.[55] have shown that fluorination starts at the defect sites of the CNT and then continues also to other sites. (2) Yue et al. have demonstrated that increasing degree of fluorination (increasing amount of defects) results in a strong decrease of the conductivity of CNT[56]. This would be in principle agreement with the data recorded: Within region II, defect states of the CNT, which are induced to an even larger extent during the milling process, are likely to be fluorinated first; the electronegative fluoride ions at these former defect sites cause the change of the binding energy of the main sp^2 carbon signal due to their strong inductive effect. However, this would not result in a further decrease of conductivity, since
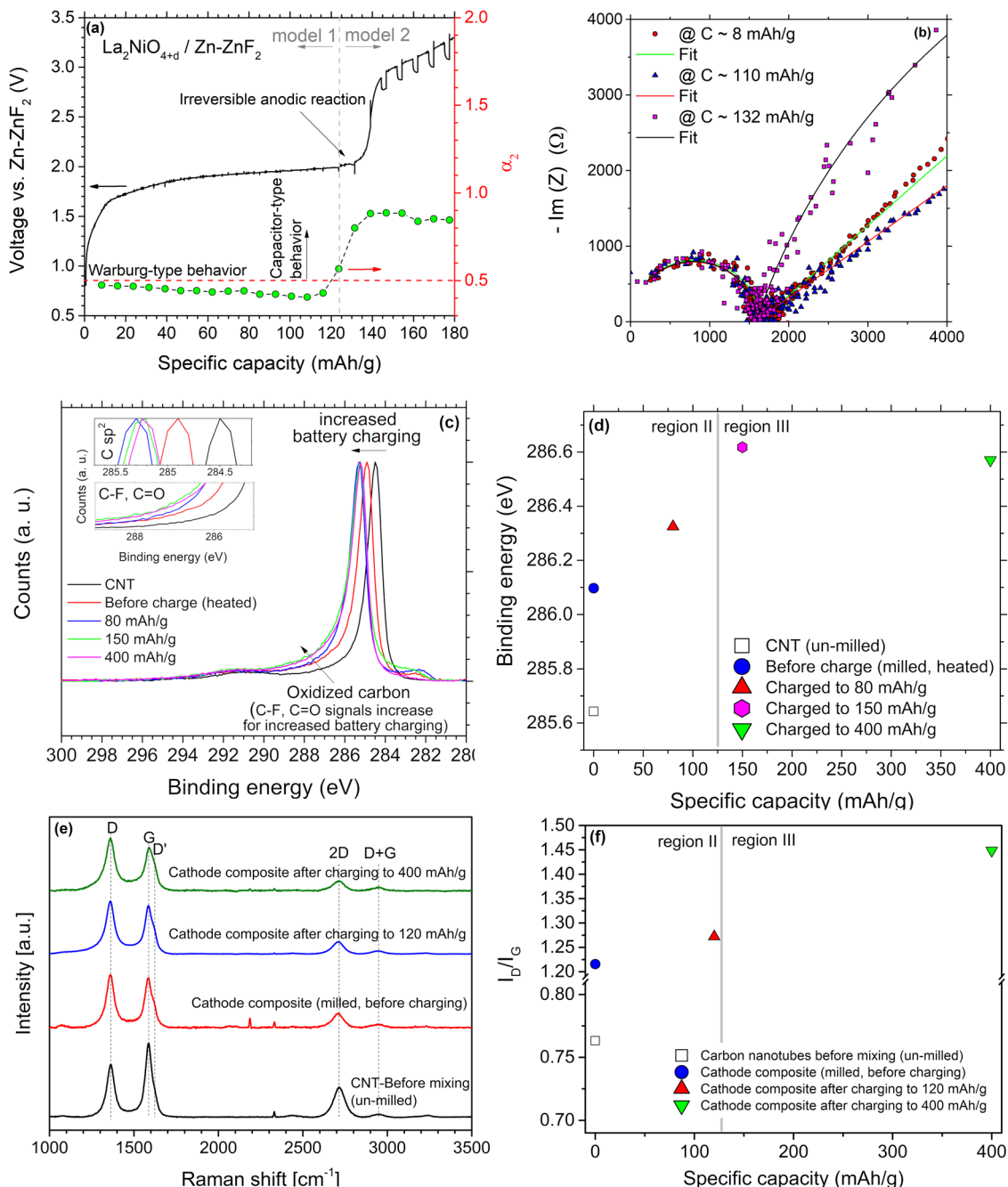
Fig. 5 State of charge-dependent impedance study of La$_2$NiO$_{4.13}$ and the role of carbon nanotube additive. a Results of the galvanostatic electrochemical impedance spectroscopy and variations of α by charging of the electrochemical cells build up from La$_2$NiO$_{4+d}$ against Zn-ZnF$_2$ anode materials at an operational temperature of 170 °C; **b** respective Nyquist curves at different charging capacities for the La$_2$NiO$_{4+d}$/Zn-ZnF$_2$ cell; **c** XPS measurements (background corrected) of the C1s emission line on the carbon nanotube before mixing/milling (CNT) and samples before charge (heated at 170 °C inside an Ar-filled glovebox for 6 h) and after charge at different cutoff capacities of 80, 150, and 400 mAh/g; **d** changes of the area-weighted average binding energy of the C1 emission versus charge capacity for CNT and the samples before (heated) and after charge; (**e**) Raman shifts for the carbon nanotubes (before mixing/milling) and the cathode composite before and after charge up to 120 and 400 mAh/g; and **f** corresponding I_D/I_G ratios obtained from the Raman shifts.

those defects had broken the sp^2 networks of the CNT already after milling. On increasing the degree of fluorination in region III (increase of oxidized carbon species), the sp^2 network of the CNT gets distorted even further by the fluorination of regular carbon sites or by affecting also the inner CNT, which would lead to an ongoing decrease of conductivity, hindering electron transfer to the active cathode material.

Clearly, the fact that the carbon matrix is changed in a side reaction on charging of the cells requires a fine-tuning of the charging and discharging conditions in order to establish reversible all-solid-state FIBs. We conclude that a reversible fluoride intercalation/deintercalation into/from La$_2$NiO$_4$ requires that the creation of further defect states within the CNT matrix has to be avoided, since the electronic conductivity of the carbon
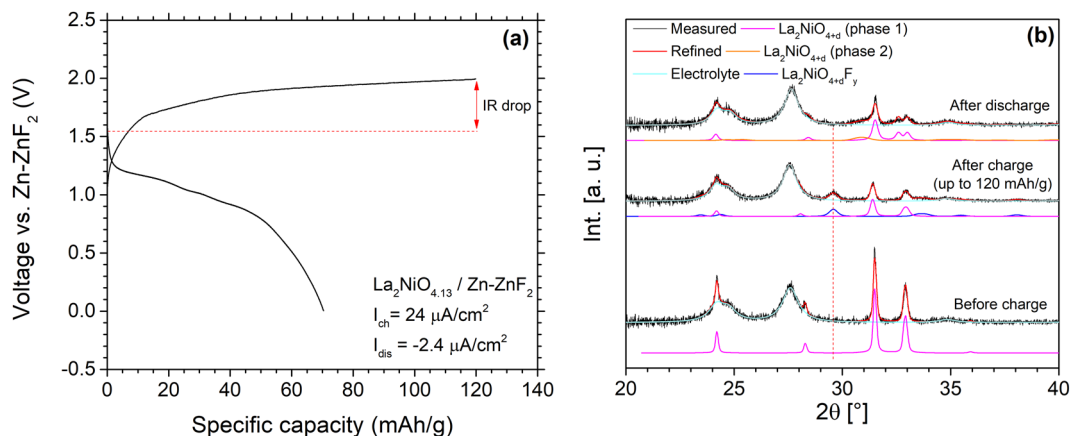
Fig. 6 Charging and discharging of La$_2$NiO$_{4.13}$. a A typical charge/discharge curve of the La$_2$NiO$_{4+d}$/Zn-ZnF$_2$ cell, which is charged up to a cutoff capacity of 120 mAh/g at operating temperature of 170 °C and charge and discharge current densities of +24 μA/cm^2 and −2.4 μA/cm^2, respectively. **b** Respective XRD patterns of La$_2$NiO$_{4+d}$ before and after charging at the same operating condition in comparison with the initial La$_2$NiO$_{4+d}$ cathode material. Details of the Rietveld refinement can be found in Supplementary Table 8.

matrix would be lowered and the transfer of electronic charge carriers to the active cathode material would be impeded. This optimization of operation conditions is described in detail in the subsequent chapter.

In addition, it is again worth emphasizing that XPS cannot be used to track the changes of the Ni oxidation state or other changes in the Ruddlesden–Popper-type phase. This originates from the fact that the particles of the active material show a strong coverage with the electrolyte and/or carbon species (see TEM images given in Fig. 3a, b and Supplementary Fig. 1 and further information on the XPS studies provided in Supplementary Discussion). Therefore, no Nickel signal could be observed, showing that the XPS spectra provide only information on the nanocrystalline carbon and electrolyte additives.

On the structural reversibility of the fluorination of La$_2$NiO$_{4.13}$/La$_2$NiO$_{4.13}$F$_{1.87}$. Figure 6a depicts a typical charge/discharge curve of a La$_2$NiO$_{4+d}$/Zn-ZnF$_2$ electrochemical cell charged to 120 mAh/g, which is discharged with a reduced discharging current of −2.4 μA/cm^2 (−1.0 μA). A drop in the discharge potential of ~0.4 V was found between the end of the charge and the beginning of the discharge. This "IR drop" is arising from the polarization coming from internal resistance (impedance) of the electrode materials[1,3]. The IR drop is followed by an extended sloping discharge plateau between ~1.2 and 0.8 V. Such sloping plateaus are commonly found for layered cathode materials for LIBs[3], indicating compositional flexibility of the various compounds. The discharge voltage plateau for the La$_2$NiO$_{4.13}$/Zn-ZnF$_2$ cell seems to be higher than the La$_2$CoO$_4$/Zn-ZnF$_2$[27] by approximately 0.4 V, showing the higher energy density of this compound from the fact that the redox potential Ni^{2+}/Ni^{4+} is higher than the redox potential Co^{2+}/Co^{3+}. Finally, toward the end of the discharge process the potential drop between 0.8 and 0 V occurs with an increasing slope.

The discharge capacity is measured to be around 70 mAh/g (Fig. 6a), which is the highest discharge capacity that has been obtained so far for an FIB with an intercalation-based cathode material (Supplementary Fig. 14 and Supplementary Table 7 summarize the discharge capacity of La$_2$NiO$_{4+d}$ as compared to the other previously studied intercalation-based cathode materials including La$_2$CoO$_4$[27,33], LaSrMnO$_4$[32], and Schafarzikite-type structure of Co$_{0.5}$Fe$_{0.5}$Sb$_2$O$_4$[31] showing the highest obtained discharge capacity for the La$_2$NiO$_{4+d}$/Zn-ZnF$_2$ electrochemical cell). Note that

such a high discharge capacity can only be found by using small discharge current density such as −2.4 μA/cm^2 (−1.0 μA). On using a higher discharge current density of −12 μA/cm, the discharge capacity reduces to ~50 mAh/g (see also Supplementary Fig. 15).

The XRD measurements show a complete disappearance of the fluorinated phase on discharging (Fig. 6b). Two phases with reduced c lattice parameter (and therefore cell volume) were found after discharging. The first phase (phase 1) is very similar to the original La$_2$NiO$_{4+d}$ before charge with similar cell volume ($V = 379.80(15)$ Å^3) and a small orthorhombic distortion ($a = 5.4598(10)$ Å, $b = 5.5097(15)$ Å, $c = 12.6256(28)$ Å). The second phase shows a strong broadening of the (103)$_{Fmmm}$ reflection, and we used a Gaussian distribution of phases with c lattice parameters ranging between 12.81 and 13.56 Å to fit this phase in the XRD pattern (which are given as a summed partial curve labeled as "phase 2" in Fig. 6b). The broad distribution of de-fluorinated phases is best explained with a small fluctuation of the strongly reduced fluorine content within this compound, in agreement with the sloping discharging plateau. After discharging, the molar ratio of phase 1 (La$_2$NiO$_{4.13}$) to phase 2 (i.e., nearly unfluorinated to strongly de-fluorinated) is about 1.5:1 and clearly distinguishes from the ratio of 2.1:1 of fluorinated La$_2$NiO$_{4.13}$F$_y$ to unfluorinated La$_2$NiO$_{4.13}$ found after charging. This shows an excellent structural reversibility of the fluorination process for La$_2$NiO$_{4.13}$. Further, the low Coulombic efficiency of this first charge/discharge capacities cycle together with the reduction of the Ruddlesden–Popper phase content at higher charging capacities is in agreement with the side reactions of the oxidation (fluorination) of the defect states of the CNT as reported in the previous chapter. This does not significantly impair the conductivity of the cell below ~2.2 V, according to the impedance spectroscopic measurements (see Fig. 5a).

Developing a highly reversible all-solid-state FIB. Taking into account the findings of the previous sections, the cycling conditions of the La$_2$NiO$_{4+d}$/Zn-ZnF$_2$ cells were optimized in order to obtain stable cycling behavior. Therefore, two cutoff criteria were set for the charging reaction: (1) a cutoff voltage of 2.3 V was chosen as a result from the potential jump shown in Fig. 2a (after which the cell builds up additional resistances most severely due to increasing amount of defect states in the CNT network as found in the impedance study). (2) Different cutoff capacities of 30, 50, 80, and 120 mAh/g were then tested in order to find the optimized charging/discharging conditions of the cell (within the
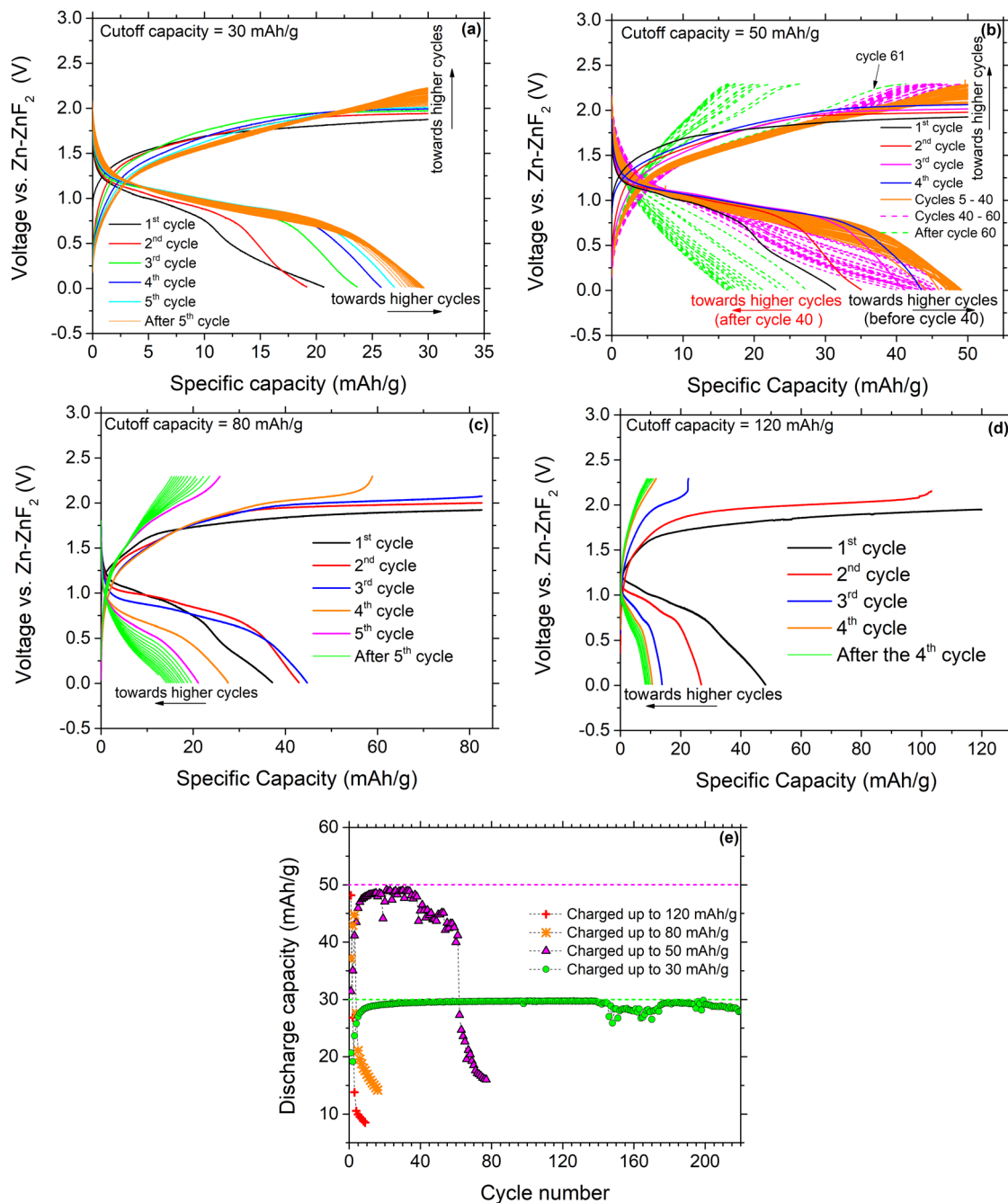
Fig. 7 Cycling behavior of La$_2$NiO$_{4.13}$. Cycling curves of the La$_2$NiO$_{4+d}$/Zn-ZnF$_2$ at $T = 170$ °C, $I_{charge} = +24\,\mu/cm^2$, $I_{discharge} = -12\,\mu/cm^2$, and cutoff charge potential $= 2.3$ V at various cutoff capacities of **a** 30 mAh/g (for better depiction, only the first 80 cycles are shown), **b** 50 mAh/g, **c** 80 mAh/g, and **d** 120 mAh/g. **e** Variation of the discharge-specific capacity with cycle number for all of the mentioned cells.

range where only already existing defects within the CNT network are impacted). Criterion (1) can only be met for samples with high cutoff capacities or at the highest cycling numbers of the cells with low cutoff capacities. For the latter, this originates from the charge efficiency slightly below 100% (98–99%, see Fig. 7), which result in a small but continuous degradation of the carbon additive. Figure 7 summarizes the electrochemical cycling behavior of the La$_2$NiO$_{4+d}$/Zn-ZnF$_2$ cells with respect to the different cutoff charge capacities.

Clearly, the choice of the cutoff charging capacity can significantly influence the cycling behavior. For the lower cutoff capacities of 30 and 50 mAh/g, the discharging capacity increases continuously to 30 and 50 mAh/g during the first 5–10 cycles (see

Fig. 7a, b, e). After those cycles, a Coulombic efficiency of on average 98–99% (average Coulombic efficiency for the whole cycling range: 97.68% and 95.44% for charge cutoff capacities of 30 and 50 mAh/g, respectively) is obtained (see Fig. 8). As discussed, the low Coulombic efficiency at the early cycle numbers originate from the presence of the side reactions on the carbon additives and show that the cells can be activated to become cycling stable by the more careful subsequent charging/discharging within the first cycles.

Interestingly, the phase behavior at extended cycling numbers is also different to what was observed for the first charging/discharging with a cutoff capacity of 120 mAh/g. At cycle number 10 (for the cell with cutoff capacity of 30 mAh/g), the XRD
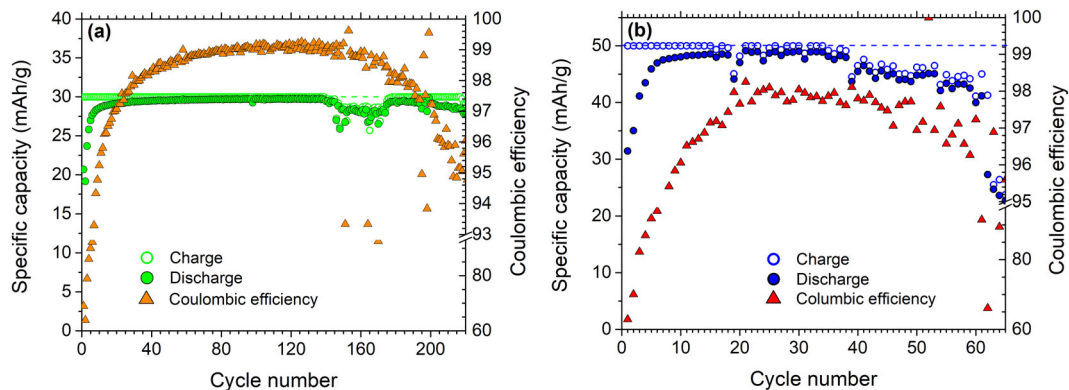
Fig. 8 Cycling stability of La$_2$NiO$_{4.13}$. Charge/discharge capacities and Coulombic efficiency against cycle number for the cells with the cutoff capacities of **a** 30 mAh/g and **b** 50 mAh/g.
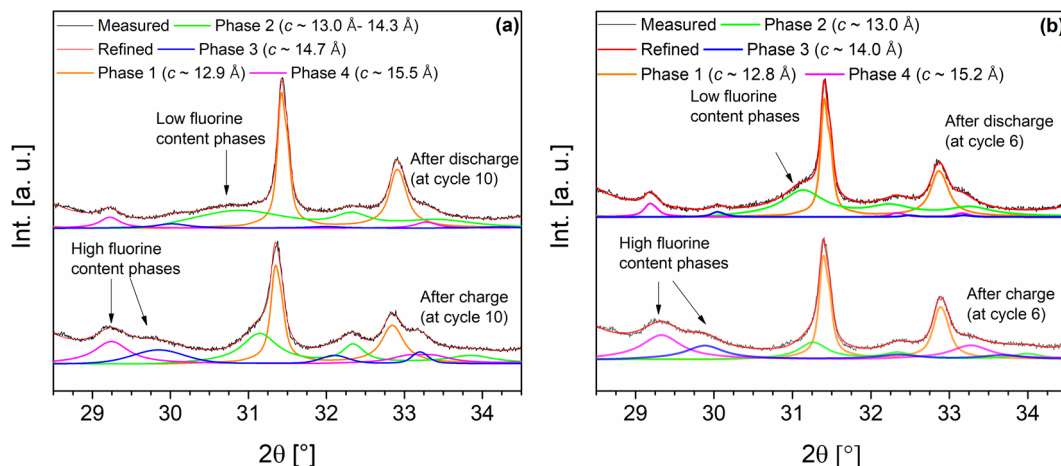
Fig. 9 Structural changes of the RP-type phase at higher cycle numbers. Excerpt of XRD measurement for La$_2$NiO$_{4+d}$/Zn-ZnF$_2$, which is charged at $T =$ 170 °C, $I_{charge} = +24\,\mu$A/cm^2, and $I_{discharge} = -12\,\mu$A/cm^2 after charge and discharge **a** at the tenth cycle for the charge cutoff of 30 mAh/g and **b** at the sixth cycle for the charge cutoff capacity of 50 mAh/g.

measurements show that 2 high fluorine content phases with increased lattice parameter c (see Fig. 9a) coexist with a few other low fluorine content phases with slightly different lattice parameter c values. These phases are shown in Fig. 9a as a single average phase (phase 2).

Quantitative calculations based on the Rietveld method show that the summation (of the relative weight percent) of the high fluorine content phases (after charge up to 30 mAh/g) are about 36%; however, approximately 13% of those high fluorine content phases can still be found after the discharge (at tenth cycle) (Table 3). Therefore, ca. 23% of the active cathode material takes part in the redox reactions, which corresponds to accommodation of ~0.45 fluoride ions into the overall available La$_2$NiO$_{4.13}$ phase (which is the amount of fluoride ions corresponding to a specific capacity of 30 mAh/g for 100% Coulombic efficiency). The same argument is true for the cell with the cutoff capacity of 50 mAh/g after the sixth cycle: the summation of the relative fraction of the high fluorine content phases is around 45% of which ca. 8% retains after the discharge (Table 3), which shows participation of roughly 38% of the active cathode material in the redox reaction corresponding to an uptake of ~0.76 F$^-$. Since a Coulombic efficiency of close to 100% (average Coulombic efficiency of 97.68% and 95.44% for charge cutoff capacities of 30 and 50 mAh/g, respectively) is found, this would mean that La$_2$NiO$_{4.13}$ would have to take up approximately two fluoride ions ([0.45/23%] ≈

[0.76/38%] ≈ 2), which is in agreement with the structural changes found from the structural and compositional analysis of the charged state by ADT, XAS, and EDX. In combination with the irreversibility of the side reaction of the carbon additives, we conclude that the charging and discharging capacities at higher cycle numbers can be fully assigned to the changes within the active cathode materials La$_2$NiO$_{4.13}$.

Therefore, it is important to note that the maximum capacity of ~100–120 mAh/g of the material can be fully accessed within the contributing particles: a limiting of the charging capacity does not result in a limited homogenous overall degree of fluorination, i.e., the grains do not change from a homogenous composition of the un-fluorinated state La$_2$NiO$_{4.13}$ to a homogenous composition of a partly fluorinated state La$_2$NiO$_{4.13}$F$_{0.45}$. Instead, the presence of highly fluorinated phases La$_2$NiO$_{4.13}$F$_{1.59}$ in addition to nearly un-fluorinated particles La$_2$NiO$_{4.13}$F$_d$ is observed experimentally. The smaller overpotentials, which can arise during the fluorination of the material, are the plausible origin why the carbon fluorination can proceed as a competing side reaction to some small extent (1–3%) at the higher cycle numbers. Without doubt, this undermines the high potential of the material to be improved further by, e.g., tailoring of the particle size/shape and/or coating of the surface in order to make the theoretical capacity fully accessible in future.

For the cutoff capacity of 30 mAh/g, the discharge capacity is highly stable at least over a range of 220 cycles with an excellent

Table 3 Changes of phase fractions of the RP-type phases at different states of charge.

	Phase 1 (low fluorine content phase) [%]	Phase 2 (low fluorine content phase) [%]	Phase 3 (high fluorine content phase) [%]	Phase 4 (high fluorine content phase) [%]	Summation of low fluorine content phases [%]	Summation of high fluorine content phases [%]
30 mAh/g/ after charge	32.7 (±5)	31.1 (±1)	26.8 (±5)	9.5 (±2)	63.5 (±7)	36.3 (±5)
30 mAh/g/after discharge	47.1 (±4)	40.51 (±6)	4.8 (±1)	7.6 (±1)	87.6 (±7)	12.4 (±1)
50 mAh/g/ after charge	38.6 (±3)	15.7 (±1)	19.4 (±1)	26.2 (±2)	54.4 (±3)	45.7 (±2)
50 mAh/g/after discharge	45.8 (±2)	46.3 (±2)	1.5 (±0.1)	6.3 (±0.3)	92.1 (±3)	7.9 (±0.3)

Relative fractions of the different phases of the $La_2NiO_{4+d}(F_y)$ active cathode material after charge and discharge against Zn-ZnF₂ (at $T = 170\,°C$, $I_{charge} = +24\,\mu A/cm^2$, and $I_{discharge} = -12\,\mu A/cm^2$) at the tenth and sixth cycle for the cutoff capacities of 30 and 50 mAh/g, respectively. Further details of the Rietveld refinement can be found in Supplementary Table 9.

Coulombic efficiency for cycle numbers >10 (97.68% in average for the whole cycling range). However, after the cycle number 140, a small capacity loss can be observed followed by some discharge capacity fluctuations; we would like to acknowledge that until then the battery was already running for almost 3 months, and it is hard to trace back the detailed origin of this small capacity loss. For the cell with the cutoff capacity of 50 mAh/g, the discharge capacity is very stable up to the cycle number 40, again with high Coulombic efficiency (95.44% in average for the whole cycling range). After the 40th cycle (up to cycle number 60), the potential within the later stage of the charging reaches closer to the cutoff potential of 2.3 V (see Fig. 7b), which results in a complementary small reduction of the Coulombic efficiency (Fig. 8b). This is in agreement with the CV studies reported in the previous section, which show that the amounts of side reactions at the CNTs increases for increasing potentials within the cell. Therefore, the closer the potential reaches to 2.3 V, the more a detrimental creation of additional defects within the CNTs occurs. Therefore, the charging capacity reduces slightly, which consequently also results in a reduction of the discharge capacity. After the 60th cycle, a significant capacity drop <30 mAh/g has been observed, which is followed by an increasing capacity fading due to continued destruction of the conductive matrix. In this context, we would like to acknowledge that an even more elaborated understanding of the details of the mechanism, which lead to a capacity fading at high cycle numbers, will require further investigations. In this context, synchrotron-based methods to elaborate the structural stability of the material might be of special interest, especially once new in situ cell designs become available.

It is worth noting that the obtained cycling performances of La_2NiO_{4+d} outperform the best cycling results for the other intercalation-based cathode materials such as La_2CoO_4 with respect to cycling stability, effective capacity, and cell potential[27] (see also Supplementary Fig. 16). The reason for the stability can be understood as a result from the limiting of the charging capacity resulting in a limited oxidation of carbon within the first few cycles facilitating the maintenance of electrically conducting interfaces. Based on this, we conclude that the slow and limited oxidation of the carbon matrix within the first cycles results in a better separation of the $La_2NiO_{4.13}/La_2NiO_{4.13}F_{1.59}$ plateau from the side reaction, which enables the high cycling stability.

It is also worth emphasizing that the charging plateau increases to higher potentials while the potential of the discharging plateau lowers on increased cycling, resulting in a decrease of energy efficiency. Apparently, this is more severe at the higher chosen cutoff capacities. This indicates that some processes continue to happen at the interfaces (e.g., electrolyte to electrode material or carbon to electrode material), which increase the internal impedance[57] of the cell and therefore lower the energy efficiency[58]. However, this could also originate from overpotentials arising within the conversion-based anode material (which suffer from much larger volume changes[27]) and must not necessarily be related to the intercalation-based cathode. This can be withdrawn from Supplementary Fig. 17, which shows cycling performance of La_2NiO_{4+d} against Pb-PbF₂. Using Pb-PbF₂ introduces smaller charge overpotentials (as compared to Zn-ZnF₂)[27] to the electrochemical system and therefore the cell can be charged up to higher cutoff capacities resulting in a higher discharge capacity (up to ~60 mAh/g) for approximately 10 cycles.

By increasing the cutoff capacity to higher values of 80 and 120 mAh/g, the capacity fading on increased cycling is higher. From Fig. 7c–e, it can be seen that for the cell with the charge cutoff capacity of 80 mAh/g the discharge capacity increases up to ~46 mAh/g after 3 cycles; however, the cell experiences a severe capacity loss afterwards. For the cell with the higher charge cutoff capacity of 120 mAh/g, the first discharge capacity was approximately around 50 mAh/g; although this is the highest discharge capacity obtained for a cell based on an intercalation-based cathode so far (at a high discharge current density of $-12\,\mu A/cm^2$), the capacity loss is even more severe. After 3 cycles, only 20% of initial discharge capacity could be recovered (Fig. 7d, e). This shows that a slow conditioning of the cells is preferable to improve their cycling behavior.

In addition, we would like to emphasize that contact loss from the active cathode material to electrolyte or carbon additives due to volume changes can also be an additional influence for capacity fading. Such influences could be previously resolved, e.g., for cathode materials for LIBs used with thiophosphate electrolytes[59], facilitated from the fact that such composites show a high density after compacting, which originates from the softness of the thiophosphate electrolytes. Attempts to analyze this aspect were also made for the La_2NiO_4 composite before and after charging to 120 mAh/g. However, in our case the composites are much more nanocrystalline, and $La_{0.9}Ba_{0.1}F_{2.9}$ do not form a dense matrix around the active particles of $La_2NiO_{4.13}$ (overall density of ~70%, see scanning electron microscopic (SEM) images provided in Supplementary Fig. 18), which prohibits a detailed analysis of this aspect. This is also in full agreement with the TEM studies (see Fig. 3a, b and Supplementary Fig. 1), which could not provide detailed information on this aspect.

In summary, it is shown that by building all-solid-state FIBs based on Ruddlesden–Popper-type La_2NiO_{4+d} as the cathode material, excellent cycling stability of such cells can be obtained. Detailed structural analysis of the single crystals (observed by STEM) of the charged/un-charged particles by means of Fast-ADT together with EDX and XAS measurements clearly show a change in the oxidation state of Ni and occupation of the anion

interlayers of La_2NiO_{4+d} by fluoride ions over electrochemical charge, revealing the origin of the charge/discharge curves. The results reveal that the cutoff criteria (cutoff charge capacity and voltage) play a vital role in the cycle life of the cell and that the formation of stable interfaces between the active material and especially carbon-based additives might play a similar role for cathode materials in FIBs than for anode materials in LIBs. Clearly, it would be important to develop strategies to increase the reversibly accessible capacity closer to the capacity of around 106 mAh/g for formation of $La_2NiO_{4.13}F_{1.59}$. This is a general problem for FIBs and known within the community also for testing new battery systems based on liquid electrolytes. Therefore, we think that (as for all-solid-state LIBs) coating techniques as well as an advanced engineering of the electrode composites could help to improve the La_2NiO_{4+d} system further. However, the high amount of fluoride ions per transition metal incorporable into La_2NiO_{4+d} highlights the importance of multivalent electrode materials for battery applications.

Methods

Preparation of the electrodes and electrolyte materials. Within this article, the terminology of the electrochemical cell components (anode and cathode material) is based on the role of the electrode on the discharge. All of the cell components including electrolyte, anode composite, and cathode composite have been synthesized via ball milling using ZrO_2 vials and balls. Note that the vial was filled and extracted inside a high purity Ar-filled (99.999%) glovebox and sealed before each milling process. The milling processes were conducted in 10-min intervals with 20-min rest between each interval (to avoid excessive local increase in temperature).

Preparation of the $La_{0.9}Ba_{0.1}F_{2.9}$ electrolyte composite: Preparation of the $La_{0.9}Ba_{0.1}F_{2.9}$ was done according to literature[60]: stoichiometric ratios of BaF_2 (STREM Chemicals, 99%) and LaF_3 (STREM Chemicals, 99.9%) were milled for 12 h at a rotational speed of 600 RPM (rounds per minute).

Preparation of the La_2NiO_{4+d} cathode composite: For preparation of the La_2NiO_{4+d} cathode composite material, first the pure $La_2NiO_{4.13}$ compound was synthesized by solid-state reactions according to previous reports[61,62]: Stoichiometric ratios of La_2O_3 (Alfa Aesar, 99.9%, pre-dried at 1200 °C for 12 h before use) and NiO (Sigma Aldrich, +99.99%, pre-dried at 700 °C for 12 h before use) were mixed and heated under air at 800 °C for 10 h. Then the mixture was hand-ground and re-heated under air at 1400 °C and kept for 4 h. The heating/cooling rates were 2 and 3 °C/min, respectively. For preparation of the La_2NiO_{4+d} cathode composite, 30 wt-% of the as-synthesized $La_2NiO_{4.13}$ was mixed with 60 wt-% of the electrolyte ($La_{0.9}Ba_{0.1}F_{2.9}$) and 10 wt-% of CNTs (dried at 190 °C under Ar) to improve the ionic and electronic conductivity of the cathode material (corresponding to volume fractions of 23 vol-% $La_2NiO_{4.13}$, 52 vol-% $La_{0.9}Ba_{0.1}F_{2.9}$, and 25 vol-% CNTs). The mixture was then ball milled for 3 h at a rotational speed of 250 RPM. Note that higher milling speed would result in amorphization of the La_2NiO_{4+d}, by that destroying the layered structure which is a prerequisite for the structural reversibility of the intercalation of fluoride ions. The stability of $La_2NiO_{4.13}$ is well confirmed with respect to the absence of significant changes of the lattice parameters of the electrolyte and electrode material after this milling process and from the quantitative phase analysis of the electrode composite (Supplementary Table 1), which agrees well with the quantity of $La_{0.9}Ba_{0.1}F_{2.9}$ and $La_2NiO_{4.13}$ in the weighted phase fractions. Further, it is worth mentioning that, after compacting, the electrode composites possess a relative porosity in the order of 30%, as described in our previous article[27].

Preparation of $Zn-ZnF_2$ anode composite: 50 wt-% of the $La_{0.9}Ba_{0.1}F_{2.9}$ electrolyte material, 20 wt-% of the Zn (ABCR, 98%), 20 wt-% of ZnF_2 (ABCR, 99%), and 10 wt-% of black carbon (dried at 190 °C under Ar) were milled for 12 h at a rotational speed of 600 RPM.

Preparation of $Pb-PbF_2$ anode composite: 45 wt-% of Pb (Sigma Aldrich, >99%), 45 wt-% of PbF_2 (STREM Chemicals, 99+), and 10 wt-% of dried black carbon were milled for 12 h at a rotational speed of 600 RPM.

Electrochemical testing. To make a battery cell, three layers of cathode/electrolyte/anode were pressed at a pressure of 2 tons for 90 s, using a desktop press (Specac) inside an Ar-filled (99.999%) glovebox. The dimensions of the cell were measured to be 1.6 and 7.3 mm for the thickness and the diameter, respectively.

Battery cells were spring-loaded (as described in ref. [32]) into a modified air-tight Swagelok-type cell with current collectors made of stainless steel. All electrochemical cells were loaded, sealed, and removed in a high purity Ar (99.999%) glovebox. However, for electrochemical testing, the sealed cells were operated outside the glovebox. To ensure sufficient mobility of the fluoride ions within the electrolyte, the electrochemical cells were heated at 170 °C. To minimize the thermal fluctuations (typically in the order of ±1 °C), the electrochemical cells were covered with glass wool and the room was held at 21 °C by an air conditioner. We would like to emphasize that this operation temperature was already optimized in a previous study[33]; at

ambient temperature, the conductivity of the electrolyte is below 10^{-6} S/cm[60], which implies an increase of the inner resistance by a factor of >100 and overpotentials >10 V for the current densities chosen, so that no charging can be obtained within a potential range of 0–3 V. On the other hand, increasing the temperature to 200 °C was found to decrease the Coulombic efficiency by a factor of 3 within our previous study on La_2CoO_4[33]. Therefore, the operation temperatures of 170 °C can be considered as an optimized choice for the operation of this class of compounds.

Battery testing was performed using a potentiostat from *BioLogic* (SP-150 or VSP300). All voltages are given as potentials against the anode material. The mass of the active cathode material La_2NiO_{4+d} was approximately 1.5 mg and anode composites were used in a 20-fold capacity excess compared to the active cathode material; in this respect, all specific capacities in this article are given with respect to the amount of the active cathode material. This composition is chosen in accordance with our experience on testing different composite compositions (an example can be found in Supplementary Fig. 19). Further, higher absolute masses result in easy delamination of the cathode side and were therefore not considered.

The electrochemical experiments were performed galvanostatically, with charging and discharging currents of +10 μA (~24 μA/cm²) and −5.0 μA (~−12 μA/cm²), respectively (unless stated otherwise). Note that the charge/discharge current density corresponds roughly to C/20 and C/40 for charge and discharge, respectively. The C-rates have been calculated based on the theoretical capacity of the active cathode material (~130 mAh/g). The discharge processes were carried out directly right after the charge. For the charging step, two cutoff criteria were chosen simultaneously: a voltage cutoff (2.3 V) or a capacity cutoff (30, 50, 80, 120 mAh/g), depending on what was reached first. The voltage cutoff criterion was chosen based on results obtained from a CV study performed at 170 °C with a scan rate of 0.1 mV/s.

Impedance spectroscopy. EIS of the cells was performed simultaneously during the galvanostatic charging at 170 °C within the frequency range between 500 kHz and 100 mHz with a current amplitude of 10 μA. The measurements were performed with 30 points per decade, averaging 5 measures per frequency.

X-ray diffraction. XRD was used for analyzing the structure and composition of the electrode composites. The measurements were performed using a Bruker D8 Advance in Bragg–Brentano geometry with Cu K_α radiation (VANTEC detector). To avoid potential side reactions with the atmosphere, all the samples were loaded into a low background specimen holder (Bruker A100B36/B37) and sealed inside an argon-filled glovebox before every measurement. Data were generally recorded in an angular range between 20° and 70° 2θ for a total measurement time of 4 h using a step size of ~0.007° and a fixed divergence slit of 0.3°. For the high-resolution measurements, the counting time was kept constant; however, the angular range was reduced to 27°–36° 2θ.

Analyses of diffraction data were performed by using the Rietveld method as implemented in TOPAS V5. The instrumental intensity distribution was determined empirically from a sort of fundamental parameters set[63] using a reference scan of LaB_6 (NIST 660a). The microstructural parameters (crystallite size and strain broadening) were refined to adjust the peak shapes. Displacement parameters were constrained to be the same for all atoms of all phases to minimize quantification errors and to account for angular-dependent intensity changes induced by absorption and surface roughness.

X-ray absorption spectroscopy. To obtain a sufficient amount sample in a charged state, 5 cells were charged to 120 mAh/g. The cathode sides were carefully scratched off (inside the Ar-filled Glovebox) and merged. La_2NiO_{4+d} ($0.030 \leq d \leq 0.17$) standards (for XAS measurements) were produced by heating stoichiometric ratios of (dried) La_2O_3 and NiO at different atmospheres. For more experimental detail concerning the XAS reference preparation, please see Supplementary Table 6 (respective XRD patterns of the standards phases and their lattice parameters can be found in Supplementary Fig. 20 and Supplementary Table 6).

X-ray absorption experiments were carried out at beamline P65 at Deutsches Elektronen-Synchrotron Desy in Hamburg (Germany). For the measurements at the Ni K-edge at 8333 eV, a Si(111) double-crystal monochromator was applied in continuous scan mode (180 s/spectrum). Owing to the low Ni concentration of the samples, spectra were recorded in fluorescence geometry using a passivated implanted planar silicon (PIPS) detector. The preparation of the samples was carried out under inert atmosphere in a glove box producing pellets diluted with boron nitride. Monochromator calibration was carried out using a Ni foil. More detailed information about data analysis are given in Supplementary Information.

Transmission electron microscopy. TEM samples were prepared by placing a drop of the powders dispersed in n-hexane on a carbon-coated copper grid. The powder from the (charged) electrode composite was the same as the one used for XAS analyses. A FEI Tecnai F30 S-TWIN transmission electron microscope equipped with a field emission gun and operated at 300 kV was used. Ten-μm condenser aperture, spot size 6, and gun lens 8 were set to produce a quasi-parallel beam with a 200-nm size for the ADT experiments. In case of the EDX spectroscopic measurements, a 50-μm condenser aperture, spot size 6, and gun lens 1 were used to increase the electron dose and have a reliable amount of counts on the EDX detector (EDAX EDAM III). STEM images were collected using a Fischione HAADF detector. Electron diffraction patterns were

acquired with an UltraScan4000 CCD camera provided by Gatan (16-bit, 4096 ×4096 pixels). Hardware binning 2 and exposure time of 2 s were used to acquire non-saturated diffraction reflections. ADT datasets were acquired with an automated acquisition module developed for FEI and JEOL microscopes, called hereby Fast-ADT, which allows the acquisition of electron diffraction tomographies in around 10 min for conventional CCD cameras and fixed tilt step of 1°[45]. Precession electron diffraction (PED)[64] was coupled to the Fast-ADT data collection to minimize the dynamical effects and improve the reflection intensity integration quality[65]. PED was generated by means of the DigiStar system developed by NanoMegas SPRL and it was kept to 1°.

Three-dimensional processing of the Fast-ADT data was done by the eADT software package[66]. Sir2014[67] was used for ab initio structure solution and Jana2006[68] was later used for crystal structure refinement. Intensity extraction for dynamical refinement was done by PETS[69]. EDX peak identification and quantification was carried out by the ES Vision software.

Scanning electron microscopy. To investigate potential microstructural changes within the electrode composites, SEM images were recorded on cross-sections of the pellet with a Philips XL30-FEG using a voltage of 30 kV. The samples were gold-coated for 40 s prior to SEM measurements.

X-ray photoelectron spectroscopy. The XPS measurements were performed by a Physical Electronic VersaProbe XPS unit with the PHI 5000 spectrometer analyzer. As the X-ray source, Al K_α radiation (1486.6 eV) with a power of 50.6 W was used. The step size and pass energy for the detailed spectra were set to 0.1 and 23.5 eV and for the survey spectra to 0.8 and 187.85 eV, respectively. As reference materials, gold and silver with the respective gold $4f_{7/2}$ (Au$4f_{7/2}$) emission line at 84.0 eV and the silver $3d_{5/2}$ (Ag$3d_{5/2}$) emission line at 368.3 eV were measured, to correct the binding energy of the spectra by the characteristic shift of the instrument. In order rule out photocurrent-induced charging of the sample, the valence band, which is dominated by the stable electrolyte phase La$_{0.9}$Ba$_{0.1}$F$_{2.9}$, was measured. Since the valence band energies were identical for the different samples, no further corrections were necessary. Further, no sputtering was done prior to and during the measurement, as well as no neutralization was necessary. For the background correction, a Shirley-type correction was used. Note that prior to XPS measurement of the uncharged sample, this sample has been heated at 170 °C for 6 h inside an Ar-filled glovebox to be more in line with the actual charging conditions.

Raman spectroscopy. Charged pellets (at 120 and 400 mAh/g) were used for Raman spectroscopy. Raman spectra were recorded with a confocal micro-Raman spectrometer Horiba HR 800 equipped with a helium-neon laser with a wavelength of 633 nm. Integral intensities were fitted using Pseudo-Voigt functions.

Density functional theory. The quantum mechanical calculations were performed in the Vienna ab initio simulation package[70], by employing the projector augmented wave[71,72] method. The calculations were based on the use of pseudopotentials and of expansion of wave function in terms of the plane wave basis set. The kinetic energy cutoff for the latter was set equal to 600 eV. The reciprocal space was sampled by Γ-centered Monkhorst–Pack-type k-mesh of $4 \times 5 \times 2$ to reflect the symmetry of the unit cell. The Perdew–Burke–Ernzerh[73] functional of GGA was used to describe the effects of exchange and correlation. The $+U$ correction, as proposed by Dudarev et al.[74], was utilized to account for the strong localization of the d-orbitals of Ni atoms. The Model employed the difference of U and J, which was chosen to be 6 eV for the d electrons of Ni atoms for all calculations on La$_2$NiO$_4$ and its fluorinated phases La$_2$NiO$_4$F$_x$. The chosen value falls within a suitable range for nickelate compounds[75,76]. During structural optimization, the forces were converged within 0.01 eV/Å on each atom. The cell lengths and ionic positions were relaxed without allowing for symmetry restrictions. The convergence of total energy during electronic self-consistency was achieved within 1×10^{-6} eV. The pseudopotentials treated 7, 11, 10, and 6 electrons, as part of the valence band of F, La, Ni, and O atoms, respectively.

Chemical fluorination. Attempts on chemical fluorination of the La$_2$NiO$_{4+d}$ has been done by different fluorinating agents: CuF$_2$ has been used as the fluorinating agent according to literature[77]. For that purpose, two separated boat-like crucibles (one was filled with CuF$_2$ and the other one with La$_2$NiO$_{4+d}$) were placed close to each other in an air-tight tube furnace under a flow of O$_2$ (0.1 SLM) and heated up at various temperatures from 200 to 350 °C for 48 h. Fluorine gas diluted with argon (10% F$_2$ by volume) was also used as the fluorinating agent at different temperatures and reaction times, which are stated directly in the figure captions (see Supplementary Fig. 4).

Data availability

All relevant data are available from the authors on request.

References

1. Goodenough, J. B. & Park, K. S. The Li-ion rechargeable battery: a perspective. *J. Am. Chem. Soc.* **135**, 1167–1176 (2013).
2. Nitta, N., Wu, F., Lee, J. T. & Yushin, G. Li-ion battery materials: present and future. *Mater. Today* **18**, 252–264 (2015).
3. Liu, C. N., G. Z & Cao, G. Understanding electrochemical potentials of cathode materials in rechargeable batteries. *Mater. Today* **19**, 109–123 (2016).
4. Vikström, H., Davidsson, S. & Höök, M. Lithium availability and future production outlooks. *Appl. Energy* **110**, 252–266 (2013).
5. Tarascon, J. M. Is lithium the new gold? *Nat. Chem.* **2**, 510 (2010).
6. Sun, C., Liu, J., Gong, Y., Wilkinson, D. P. & Zhang, J. Recent advances in all-solid-state rechargeable lithium batteries. *Nano Energy* **33**, 363–386 (2017).
7. Mauger, A., Armand, M., Julien, C. M. & Zaghib, K. Challenges and issues facing lithium metal for solid-state rechargeable batteries. *J. Power Sources* **353**, 333–342 (2017).
8. Lin, D., Liu, Y. & Cui, Y. Reviving the lithium metal anode for high-energy batteries. *Nat. Nanotechnol.* **12**, 194–206 (2017).
9. Lide, D. R. *CRC Handbook of Chemistry and Physics Internet Version 2005 Edtion* (CRC Press, 2005).
10. Gschwind, F. et al. Fluoride ion batteries: theoretical performance, safety, toxicity, and a combinatorial screening of new electrodes. *J. Fluorine Chem.* **182**, 76–90 (2016).
11. Kennedy, J. H. & Hunter, J. C. Thin-film galvanic cell Pb/PbF$_2$/PbF$_2$,CuF$_2$/Cu. *J. Electrochem. Soc.* **123**, 10–14 (1976).
12. Schoonman, J. A solid-state galvanic cell with fluoride-conducting electrolytes. *J. Electrochem. Soc.* **123**, 1772–1775 (1976).
13. Anji Reddy, M. & Fichtner, M. Batteries based on fluoride shuttle. *J. Mater. Chem.* **21**, 17059–17062 (2011).
14. Mohammad, I., Witter, R., Fichtner, M. & Anji Reddy, M. Room-temperature, rechargeable solid-state fluoride-ion batteries. *ACS Appl. Energy Mater.* **1**, 4766–4775 (2018).
15. Grenier, A. et al. Solid fluoride electrolytes and their composite with carbon: issues and challenges for rechargeable solid state fluoride-ion batteries. *J. Phys. Chem. C* **121**, 24962–24970 (2017).
16. Gschwind, F., Zao-Karger, Z. & Fichtner, M. A fluoride-doped PEG matrix as an electrolyte for anion transportation in a room-temperature fluoride ion battery. *J. Mater. Chem. A* **2**, 1214–1218 (2014).
17. Anji Reddy, M. & Fichtner, M. in *Handbook of Solid State Batteries* (eds Dudney, N. J., West, W. C. & Nanda, J.) Ch. 8 (WORLD SCIENTIFIC, 2015).
18. Düvel, A., Bednarcik, J., Šepelák, V. & Heitjans, P. Mechanosynthesis of the fast fluoride ion conductor Ba$_{1-x}$LaxF$_{2+x}$: from the fluorite to the tysonite structure. *J. Phys. Chem. C* **118**, 7117–7129 (2014).
19. Davis, V. K. et al. Room-temperature cycling of metal fluoride electrodes: liquid electrolytes for high-energy fluoride ion cells. *Science* **362**, 1144–1148 (2018).
20. Konishi, H., Minato, T., Abe, T. & Ogumi, Z. Triphenylboroxine and triphenylborane as anion acceptors for electrolyte in fluoride shuttle batteries. *Chem. Lett.* **47**, 1346–1349 (2018).
21. Zhang, L., Reddy, M. A. & Fichtner, M. Electrochemical performance of all solid-state fluoride-ion batteries based on thin-film electrolyte using alternative conductive additives and anodes. *J. Solid State Electrochem.* **22**, 997–1006 (2018).
22. Grenier, A., Porras Gutierrez, A. G., Groult, H. & Dambournet, D. Modified coin cells to evaluate the electrochemical properties of solid-state fluoride-ion batteries at 150°C. *J. Fluorine Chem.* **191**, 23–28 (2016).
23. Thieu, D. T. et al. CuF$_2$ as reversible cathode for fluoride ion batteries. *Adv. Funct. Mater.* **27**, 1701051 (2017).
24. Rongeat, C., Anji Reddy, M., Diemant, T., Behm, R. J. & Fichtner, M. Development of new anode composite materials for fluoride ion batteries. *J. Mater. Chem. A* **2**, 20861–20872 (2014).
25. Konishi, H., Minato, T., Abe, T. & Ogumi, Z. Electrochemical properties of lead fluoride electrode in fluoride shuttle battery. *J. Electroanal. Chem.* **826**, 60–64 (2018).
26. Grenier, A. et al. Electrochemical reactions in fluoride-ion batteries: mechanistic insights from pair distribution function analysis. *J. Mater. Chem. A* **5**, 15700–15705 (2017).
27. Nowroozi, M. A. & Clemens, O. Insights on the behavior of conversion based anode materials for fluoride ion batteries by testing against an intercalation-based reference cathode. *ACS Appl. Energy Mater.* **1**, 6626–6637 (2018).
28. Liu, Y., Wang, J., Xu, Y., Zhu, Y., Bigio, D. & Wang, C. Lithium–tellurium batteries based on tellurium/porous carbon composite. *J. Mater. Chem. A* **2**, 12201–12207 (2014).
29. Nowroozi, M. A. & Clemens, O. Insights on the behavior of conversion-based anode materials for fluoride ion batteries by testing against an intercalation-based reference cathode. *ACS Appl. Energy Mater.* **1**, 6626–6637 (2018).
30. Clemens, O., Rongeat, C., Reddy, M. A., Giehr, A., Fichtner, M. & Hahn, H. Electrochemical fluorination of perovskite type BaFeO$_{2.5}$. *Dalton Trans.* **43**, 15771–15778 (2014).

31. Nowroozi, M. A., de Laune, B. & Clemens, O. Reversible electrochemical intercalation and deintercalation of fluoride ions into host lattices with Schafarzikite-type structure. *ChemistryOpen* **7**, 617–623 (2018).

32. Nowroozi, M. A., Wissel, K., Rohrer, J., Munnangi, A. R. & Clemens, O. LaSrMnO4: reversible electrochemical intercalation of fluoride ions in the context of fluoride ion batteries. *Chem. Mater.* **29**, 3441–3453 (2017).

33. Nowroozi, M. A., Ivlev, S., Rohrer, J. & Clemens, O. La2CoO4: a new intercalation based cathode material for fluoride ion batteries with improved cycling stability. *J. Mater. Chem. A* **6**, 4658–4669 (2018).

34. Wissel, K. et al. Developing intercalation based anode materials for fluoride-ion batteries: topochemical reduction of $Sr_2TiO_3F_2$ via a hydride based defluorination process. *J. Mater. Chem. A* **6**, 22013–22026 (2018).

35. Ishihara, T. *Perovskite Oxide for Solid Oxide Fuel Cells* (Springer, 2009).

36. Aikens, L. D., Li, R. K. & Greaves, C. The synthesis and structure of a new oxide fluoride, $LaSrMnO_4F$, with staged fluorine insertion. *Chem. Commun.* **21**, 2129–2130 (2000).

37. Wang, L., Chen, B., Ma, J., Cui, G. & Chen, L. Reviving lithium cobalt oxide-based lithium secondary batteries-toward a higher energy density. *Chem. Soc. Rev.* **47**, 6505–6602 (2018).

38. Rice, D. E. & Buttrey, D. J. An X-ray diffraction study of the oxygen content phase diagram of $La_2NiO_{4+\delta}$. *J. Solid State Chem.* **105**, 197–210 (1993).

39. Linden, D. & Reddy, T. B. *Handbook of Batteries* 3rd edn (McGraw-Hill, 2001).

40. Rodríguez-Carvajal, J., Fernández-Díaz, M. T. & Martínez, J. L. Neutron diffraction study on structural and magnetic properties of La_2NiO_4. *J. Phys. Condens. Matter* **3**, 3215–3234 (1991).

41. Wissel, K. et al. Topochemical fluorination of La_2NiO_{4+d}: unprecedented ordering of oxide and fluoride ions in $La_2NiO_3F_2$. *Inorg. Chem.* **57**, 6549–6560 (2018).

42. Francesconi, M. G. & Greaves, C. Anion substitutions and insertions in copper oxide superconductors. *Supercond. Sci. Technol.* **10**, A29 (1997).

43. McCabe, E. E. & Greaves, C. Review: Fluorine insertion reactions into pre-formed metal oxides. *J. Fluorine Chem.* **128**, 448–458 (2007).

44. Clemens, O. & Slater, P. R. Topochemical modifications of mixed metal oxide compounds by low-temperature fluorination routes. *Rev. Inorg. Chem.* **33**, 105–117 (2013).

45. Kolb, U., Gorelik, T., Kubel, C., Otten, M. T. & Hubert, D. Towards automated diffraction tomography: Part I-Data acquisition. *Ultramicroscopy* **107**, 507–513 (2007).

46. Palatinus, L., Petricek, V. & Correa, C. A. Structure refinement using precession electron diffraction tomography and dynamical diffraction: theory and implementation. *Acta Crystallogr. A Found. Adv.* **71**, 235–244 (2015).

47. Shannon, R. D. Revised effective ionic radii and systematic studies of interatomic distances in halides and chalcogenides. *Acta Crystallogr. Sect. A Found. Crystallogr.* **32**, 751–767 (1976).

48. Andre, D., Meiler, M., Steiner, K., Wimmer, C., Soczka-Guth, T. & Sauer, D. U. Characterization of high-power lithium-ion batteries by electrochemical impedance spectroscopy. I. Experimental investigation. *J Power Sources* **196**, 5334–5341 (2011).

49. Barsoukov, E. & Macdonald, J. R. *Impedance Spectroscopy, Theory Experiment and Applications* 2nd edn (John Wiley & Sons, Inc., 2005).

50. Moulder, J. F., Stickle, W. F., Sobol, P. E. & Bomben, K. D. *Handbook of X Ray Photoelectron Spectroscopy: A Reference Book of Standard Spectra for Identification and Interpretation of XPS Data* (Physical Electronics, 1995).

51. Nansé, G., Papirer, E., Fioux, P., Moguet, F. & Tressaud, A. Fluorination of carbon blacks: an X-ray photoelectron spectroscopy study: I. A literature review of XPS studies of fluorinated carbons. XPS investigation of some reference compounds. *Carbon* **35**, 175–194 (1997).

52. Bokobza, L., Bruneel, J.-L. & Couzi, M. Raman spectroscopy as a tool for the analysis of carbon-based materials (highly oriented pyrolitic graphite, multilayer graphene and multiwall carbon nanotubes) and of some of their elastomeric composites. *Vib. Spectrosc.* **74**, 57–63 (2014).

53. Kalita, G. et al. Fluorination of multi-walled carbon nanotubes (MWNTs) via surface wave microwave (SW-MW) plasma treatment. *Phys. E* **41**, 299–303 (2008).

54. Marcoux, P. R. et al. A spectroscopic study of the fluorination and defluorination reactions on single-walled carbon nanotubes. *Phys. Chem. Chem. Phys.* **4**, 2278–2285 (2002).

55. Li, Y. et al. Fluorinated multi-walled carbon nanotubes as cathode materials of lithium and sodium primary batteries: effect of graphitization of carbon nanotubes. *J. Mater. Chem. A* **7**, 7128–7137 (2019).

56. Yue, H., Zhang, W., Liu, H., Liu, Z., Zhong, G. & Yang, Y. Synthesis and characterization of fluorinated carbon nanotubes for lithium primary batteries with high power density. *Nanotechnology* **24**, 424003 (2013).

57. Zhang, Y. C., Wang, C. Y. & Tang, X. D. Cycling degradation of an automotive LiFePO4 lithium-ion battery. *J. Power Sources* **196**, 1513–1520 (2011).

58. Du, M. J., Liao, K. M., Lu, Q. & Shao, Z. P. Recent advances in the interface engineering of solid-state Li-ion batteries with artificial buffer layers:

59. Koerver, R. et al. Capacity fade in solid-state batteries: interphase formation and chemomechanical processes in nickel-rich layered oxide cathodes and lithium thiophosphate solid electrolytes. *Chem. Mater.* **29**, 5574–5582 (2017).

60. Rongeat, C., Anji Reddy, M., Witter, R. & Fichtner, M. Solid electrolytes for fluoride ion batteries: ionic conductivity in polycrystalline tysonite-type fluorides. *ACS Appl. Mater. Interfaces* **6**, 2103–2110 (2014).

61. Sáez Puche, R., Rodriguez, J. L. & Fernández, F. Non-stoichiometric aspects and physical properties of La_2NiO_4 oxide. *Inorg. Chim. Acta* **140**, 151–153 (1987).

62. Matsuda, M., Hashimoto, M., Matsunaga, C., Suzuki, T. S., Sakka, Y. & Uchikoshi, T. Electrophoretic fabrication of a-b plane oriented La_2NiO_4 cathode onto electrolyte in strong magnetic field for low-temperature operating solid oxide fuel cell. *J. Eur. Ceram. Soc.* **36**, 4077–4082 (2016).

63. Cheary, R. W., Coelho, A. A. & Cline, J. P. Fundamental parameters line profile fitting in laboratory diffractometers. *J. Res. Natl Inst. Stand. Technol.* **109**, 1–25 (2004).

64. Vincent, R. & Midgley, P. A. Double conical beam-rocking system for measurement of integrated electron diffraction intensities. *Ultramicroscopy* **53**, 271–282 (1994).

65. Mugnaioli, E., Gorelik, T. & Kolb, U. "Ab initio" structure solution from electron diffraction data obtained by a combination of automated diffraction tomography and precession technique. *Ultramicroscopy* **109**, 758–765 (2009).

66. Kolb, U., Mugnaioli, E. & Gorelik, T. E. Automated electron diffraction tomography - a new tool for nano crystal structure analysis. *Cryst. Res. Technol.* **46**, 542–554 (2011).

67. Burla, M. C. et al. Crystal structure determination and refinement via SIR2014. *J. Appl. Crystallogr.* **48**, 306–309 (2015).

68. Petříček, V., Dušek, M. & Palatinus, L. Crystallographic computing system JANA2006: general features. *Z. Krist. Cryst. Mater.* **229**, 345–352 (2014).

69. Palatinus, L. PETS. Program for analysis of electron diffraction data, version 2.0 http://pets.fzu.cz/ (2011).

70. Kresse, G. & Furthmuller, J. Efficiency of ab-initio total energy calculations for metals and semiconductors using a plane-wave basis set. *Comput. Mater. Sci.* **6**, 15–50 (1996).

71. Kresse, G. & Joubert, D. From ultrasoft pseudopotentials to the projector augmented-wave method. *Phys. Rev. B* **59**, 1758–1775 (1999).

72. Blöchl, P. E. Projector augmented-wave method. *Phys. Rev. B* **50**, 17953–17979 (1994).

73. Perdew, J. P., Burke, K. & Ernzerhof, M. Generalized gradient approximation made simple. *Phys. Rev. Lett.* **77**, 3865–3868 (1996).

74. Dudarev, S. L., Botton, G. A., Savrasov, S. Y., Humphreys, C. J. & Sutton, A. P. Electron-energy-loss spectra and the structural stability of nickel oxide: an LSDA+U study. *Phys. Rev. B* **57**, 1505–1509 (1998).

75. Anisimov, V. & Izyumov, Y. *Electronic Structure of Strongly Correlated Materials* (Springer, Berlin, Heidelberg, 2010).

76. Pardo, V. & Pickett, W. E. Pressure-induced metal-insulator and spin-state transition in low-valence layered nickelates. *Phys. Rev. B* **85**, 045111 (2012).

77. Zhang, R., Senn, M. S. & Hayward, M. A. Directed lifting of inversion symmetry in Ruddlesden–Popper oxide–fluorides: toward ferroelectric and multiferroic behavior. *Chem. Mater.* **28**, 8399–8406 (2016).

Acknowledgements

Author contributions

M.A.N.: writing the manuscript, performed and organized the main part of the study, synthesis of the precursors, preparation of electrochemical cells and samples for further measurements, XRD measurements, electrochemical measurements (galvanostatic cycling, cyclic voltammetry, impedance spectroscopy, etc.), analysis of the data, and plotting of figures. K.W.: Raman spectroscopy. M.D.: XPS measurements and analysis of the respective data. N.H.: chemical fluorination of La_2NiO_{4+d} by CuF_2 and preparation of references La_2NiO_{4+d} ($4.03 \leq d \leq 4.17$) for XAS measurements. S.P.-R. and U.K.: TEM, EDX, and ADT measurements and analysis of the respective data. R.S. and M.B.: XANES measurements and analysis of the respective data. A.M.M. and J.R.: DFT calculations and respective discussions. S.I. and F.K.: chemical fluorination of La_2NiO_{4+d} by F_2. O.C.: designed the study and supervised the project, scientific contributor, and scientific proofing of the manuscript.

Competing interests

The authors declare no competing interests.

Additional information

Supplementary information is available for this paper at https://doi.org/10.1038/s43246-020-0030-5.

Correspondence and requests for materials should be addressed to O.C.

Reprints and permission information is available at http://www.nature.com/reprints

Publisher's note Springer Nature remains neutral with regard to jurisdictional claims in published maps and institutional affiliations.